Deconvolution of ASCA X-ray data: II. Radial temperature and metallicity profiles for 106 galaxy clusters

D.A. White
Institute of Astronomy, Madingley Road, Cambridge CB3 OHA. (E-mail: daw@ast.cam.ac.uk)

ABSTRACT

In Paper-I we presented a methodology to recover the spatial variations of properties of the intracluster gas from *ASCA* X-ray satellite observations of galaxy clusters. We verified the correctness of this procedure by applying it to simulated cluster datasets which we had subjected to the various contaminants common in *ASCA* data. In this paper we present the results which we obtain when we apply this method to real galaxy cluster observations. We determine broad-band temperature and cooling-flow mass-deposition rates for the 106 clusters in our sample, and obtain temperature, abundance and emissivity profiles (*i.e.* at least two annular bins) for 98 of these clusters. We find that 90 percent of these temperature profiles are consistent with isothermality at the 3-σ confidence level. This conflicts with the prevalence of steeply-declining cluster temperature profiles found by Markevitch et al. (1998) from a sample of 30 clusters. In Paper-III (in preparation) we utilise our temperature and emissivity profiles to determine radial hydrostatic-mass properties for a subsample of the clusters presented in this paper.

Key words: methods: data analysis – X-rays: galaxies – galaxies: intergalactic medium – galaxies: fundamental parameters – galaxies: cooling flows

1 INTRODUCTION

In Paper-I White & Buote (1999) we described our spectral-imaging deconvolution (*SID*) procedure which was developed to recover spatial variations in the intracluster gas properties from *ASCA* satellite observations. Such a procedure is required because the X-ray mirrors of this satellite have a point-spread function (PSF) which varies considerably with position and, in particular, energy. This corrupts the observed spectral properties of any extended source, *e.g.* a galaxy cluster, to the extent that any uncorrected spatially-resolved spectral analysis will yield erroneous results. Takahashi et al. (1995) showed that without correction an isothermal cluster may appear to have a temperature profile which increases with radius.

Our motivation was to create a procedure which would correct for this effect and allow us obtain temperature, and thereby mass, profiles for a large number of clusters. We also wished to address the claim made by Markevitch et al. (1998) (hereafter *MFSV*) for the ubiquitous nature of temperature declines. With a sample of 30 objects *MFSV* parameterised the average temperature decline in clusters with a polytropic index of $\gamma = 1.24^{+0.20}_{-0.12}$, *i.e.* $\Gamma \sim 4/3$. This result, if correct, is of great importance as it has been generally been assumed that clusters are isothermal.

Steeply declining temperature profiles not only complicate the interpretation of the temperature function, but also exacerbates the

discrepancy between the average baryon fraction in clusters and the mean value of the Universe expected from primordial nucleosynthesis calculations. For a Flat Universe the mean baryon fraction is calculated to be $0.06h_{50}^{-2}$ Walker et al. (1991), whereas the typical baryon content of galaxy clusters determined from X-ray data (*e.g.* White & Fabian 1995; Ettori & Fabian 1998) is $0.1 - 0.2h_{50}^{-3/2}$. This disparity, which was first highlighted by White et al. (1993), can be resolved by moving to an Open Universe model (ignoring a contribution from Ω_Λ), *i.e.* with values of $\Omega_0 \approx 0.2 - 0.3$. However, declining temperature profiles imply less gravitational mass than equivalent isothermal profiles, which leads to an increase in the generic cluster baryon-fraction estimate, and a further decrease in the implied value of Ω_0.

In addition, *MFSV* found that the average gradient is close to, and consistent with (at 2-σ), the convective instability boundary at $\Gamma \geq 5/3$. While such instabilities could result from merger activity, the ubiquitous nature of temperature declines implies that most of the clusters in their sample are disturbed. However, *MFSV* also found that approximately 60 percent of their sample exhibited evidence for cooling flow activity. As cooling flows are found in relaxed clusters [Buote & Tsai (1996); *e.g.* see Fig. 7 where they plot the mass-flow rate against the ratio of the quadrapole to monopole moments of the *ROSAT* images of clusters, and Buote (1998) where they quantify the relationship between the ratio of these moments

and the dynamical state of a cluster], these two observations are contradictory.

Further doubts have been raised by Irwin, Bregman, & Evrard (1998) following their comparison of *MFSV* results with the work from other authors (*i.e.* Ikebe et al. 1997: A780; Fujita et al. 1996: A399 and A401; Ezawa et al. 1997: AWM7; Ohashi et al. 1997: 3A0336+098, MKW3s, A1795 and PKS2354−35). Most of these other studies find isothermal temperature profiles, even for those where *MFSV* find a temperature decline. Irwin et al. also presented their own investigation of *ROSAT* colour profiles of many of the clusters in the *MFSV* sample, and they found that these were generally consisent with isothermal temperature profiles (excluding the core regions of cooling flows), even in clusters common to the *MFSV* analysis.

Recently, temperature profiles determinations have been derived from Beppo-SAX data (A2319 – Molendi et al. 1999; Virgo – D'Acri, Grandi, & Molendi 1998; Molendi 1998). Although the data from this satellite also require correction for a broad (half-power radius of $1 - 2 \, \mathrm{arcmin}$, depending on the detector) spatial point-spread function (PSF), the PSF does not vary strongly with energy (thus even without correction the SAX data could, in principle, be anlysed to correctly determine whether a cluster is isothermal or not). Of the SAX results listed above, the Virgo and Perseus cluster data only cover the cooling flow regions, while A2319 is not a cooling flow and appears isothermal in the SAX data. However, the authors are reluctant to claim any disparity with the Markevitch et al. results on the basis of this one cluster observation.

Given the above results and the issues discussed, it is clear that the *MFSV ASCA* results need to be checked by independent means. Before we discuss our analysis we shall describe the method used by *MFSV*, and compare the relative advantages and disadvantages.

The procedure used by *MFSV* requires an initial assumption for the cluster spectrum and the spatial emissivity profile. By convolving these with the energy- and position-dependent PSF they produce a spectral-image model for the cluster which they compare with the observational data. After modifying the source spectrum at different positions they attempt converge to consistency between the model and data. The disadvantages of this method are that they need to assume a source spectum and that they require a constraint on the spatial distribution of counts, *i.e.* the emissivity profile. The latter they obtain from *ROSAT* data, however the energy range of X-rays detected by *ROSAT* is much softer ($0.2 - 2 \, \mathrm{keV}$) than that used in the analysis of *ASCA* datasets (*MFSV* use $\sim 2 - 10 \, \mathrm{keV}$ photons), and so the question arises as to whether the emissivity profile of the cluster in the *ROSAT* energy band is suitable for use as a constraint in the *ASCA* data analysis. For clusters where the spectrum changes significantly between these two energy bands, *i.e.* in clusters which have a strong cooling flow, excess absorption in the core region (White et al. 1991), or even a strong temperature decline, this assumption is questionable.

In the following sections we present the results from our own analysis of *ASCA* GIS data, using the spectral-imaging deconvolution method which we described in Paper-I (White & Buote). This method is essentially non-parametric as it does not require the spectrum of the object to be specified, nor external (*ROSAT*) data to describe the emissivity profile. The main assumption of our method, namely that a fixed spatially-invariant PSF may be used for the image deconvolution has been tested for in Paper-I and shown to have a negligible impact on the results. Our other tests in that paper also show that the method can be used on observational data contaminated by events from the cosmic and instrumental background. We are confident that our procedure can reliably extract the intrinsic radial properties of the ICM for a large number of clusters, and so we have applied it to GIS data on 106 galaxy clusters observed by *ASCA*. Our methodolgy yields temperature and abundance profiles (*i.e.* at least 2 annular bins) for 92 percent (98 clusters) of the sample.

2 SAMPLE

In compiling this sample of 106 clusters we have attempted to obtain temperature profiles for as many clusters as possible. Although this sample has not been selected according a flux limit we have deliberately tried to include the 50 brightest clusters (Edge et al. 1990) (only a couple are missing), and all those clusters which were analysed by *MFSV*.

All our data are pipeline-processed observations which have been obtained from the HEASARC database[⋆] at the Goddard Space Flight Centre. Some of the GIS3 data (*i.e.* A478, A586, A2029, A2142, A2063, and 2A0336) were affected by problems with the analogue-to-digital converter and we have eliminated the GIS3 results (as results from these data are generally discrepant with the GIS2 results at large radii). Any contaminating sources which were evident in the original GIS images were masked-out before the deconvolution analysis[†]. As we analyse our spectra in circularly symmetric annuli we have implicitly assumed spherical symmetry. However, some of the clusters in our sample are clearly assymetric[‡], even within the limited spatial resolution of *ASCA*. This should be bourne in mind when interpreting the results from these clusters.

The range of background-subtracted fluxes in our sample is approximately 1,000 to several 100,000 counts, and count rates of 0.04 to $15 \, \mathrm{cts \, s^{-1}}$. The detailed numbers (from the non-deconvolved data within $20 \, \mathrm{arcmin}$ of the centre of the field, or the maximum radius above that background) are given in Table 1, together with details on the observation sequence number used and the exposure, after cleaning the event list, of the observation.

[⋆] http://heasarc.gsfc.nasa.gov/W3Browse/
[†] Cluster requiring source contamination removal were: A85, A370, A400, A665, A697, A854, A1413, A1763, A1775, A1795, A1835, A1895, A1995, A2034, A2063, A2029, A2104, A2142, A2219, A2440, A2634, A2811, A3391, A3558, A3562, AWM4, Klemola 44, MKW4s MKW9, and SC1327 (Shapley).
[‡] Clusters with some notable asymmetry in the GIS images: A539 (two core sources), A2151 (possible subtructure or contaminating source on one side of the cluster at larger radii), A2256 (subcluster merger apparent through elongated core), A2319 (offset of core with respect to the outer regions), A2440 (possible multiple core sources), A3266 (slightly offset core), A3376 (elongated), A3627 (elongated), Ophuichus (core offset) and Cygnus-A (AGN point source and offset core with respect to outer regions of cluster).

Table 1. Observational Dataset Statistics

#	Object	Sequence Number	Inst.	Exposure (k.sec.)	Cluster Counts	Count Rate
1	A85	81024000	G3	27.89	54,641	1.959
			G2	27.89	55,400	1.987
		81024010	G2	13.35	24,108	1.806
			G3	13.35	27,161	2.034
2	A119	83045000	G2	35.42	26,367	0.744
			G3	35.41	26,902	0.760
3	A262	81031000	G2	21.51	18,747	0.871
			G3	21.51	21,887	1.017
4	A370	80010000	G3	35.60	1,924	0.054
			G2	35.61	1,698	0.048
5	A399	82008000	G2	29.76	24,422	0.821
			G3	29.76	24,396	0.820
6	A400	83037000	G2	51.43	16,897	0.329
			G3	51.40	19,288	0.375
7	A401	82010000	G2	32.87	48,468	1.475
			G3	32.87	49,866	1.517
8	A426	80007000	G2	16.81	245,322	14.598
			G3	16.80	281,366	16.744
9	A478	81015000	G2	34.39	50,480	1.468
10	A496	80003000	G2	40.05	66,827	1.669
			G3	39.99	75,115	1.879
11	A521	84071000	G2	42.71	4,800	0.112
			G3	42.78	5,685	0.133
12	A539	83003000	G2	32.68	16,250	0.497
			G3	32.68	18,326	0.561
13	A548	84034000	G2	28.40	7,884	0.278
			G3	28.36	8,212	0.290
14	A576	84001000	G2	48.56	25,222	0.519
			G3	48.53	29,476	0.607
15	A586	81009010	G2	18.33	3,470	0.189
16	A611	84063000	G2	56.98	4,340	0.076
			G3	56.98	4,493	0.079
17	A644	83022000	G2	57.50	60,991	1.061
			G3	57.50	70,044	1.218
18	A665	80035000	G3	40.03	9,835	0.246
			G2	40.05	10,473	0.261
19	A697	84031000	G2	65.86	8,183	0.124
			G3	65.85	10,731	0.163
20	A754	82057000	G2	21.60	40,426	1.872
			G3	21.77	46,503	2.136
21	A773	82001000	G2	41.10	5,055	0.123
			G3	41.09	6,552	0.159
22	A780	80015000	G3	18.64	20,003	1.073
			G2	18.64	20,646	1.107
23	A854	83006000	G2	45.99	3,571	0.078
			G3	45.99	3,744	0.081
24	A963	80000000	G2	30.31	4,553	0.150
			G3	30.31	5,537	0.183
25	A990	84070000	G3	74.07	14,236	0.192
			G2	74.33	12,493	0.168
26	A1060	80004000	G2	34.72	50,897	1.466
			G3	34.70	50,315	1.450

Table 1. Observational Dataset Statistics – contd.

#	Object	Sequence Number	Inst.	Exposure (k.sec.)	Cluster Counts	Count Rate
27	A1068	84064000	G3	35.63	9,234	0.259
			G2	35.64	7,651	0.215
28	A1204	82002000	G2	32.37	3,502	0.108
			G3	32.36	4,696	0.145
29	A1246	83007000	G2	42.19	4,469	0.106
			G3	41.67	5,185	0.124
30	A1367	81029000	G2	10.62	8,863	0.834
			G3	10.62	10,066	0.947
		81029010	G3	8.61	8,250	0.959
			G2	8.61	7,527	0.875
		81030000	G2	7.94	7,184	0.905
			G3	7.94	7,693	0.969
		81030010	G2	10.75	9,848	0.916
			G3	10.75	9,857	0.917
31	A1413	81008000	G3	37.51	15,388	0.410
			G2	37.51	16,237	0.433
32	A1553	84069000	G2	34.62	9,220	0.266
			G3	34.63	10,822	0.313
33	A1576	83014000	G2	39.65	2,504	0.063
			G3	39.65	3,141	0.079
34	A1650	84021000	G2	55.08	31,696	0.575
			G3	55.13	37,382	0.678
35	A1651	82036000	G2	35.59	20,878	0.587
			G3	35.58	25,782	0.725
36	A1656	80016000	G2	7.75	44,653	5.760
			G3	7.75	45,159	5.825
37	A1682	84075000	G2	39.32	3,946	0.100
			G3	39.34	4,806	0.122
38	A1689	80005000	G2	38.15	20,542	0.538
			G3	38.15	21,708	0.569
39	A1704	81007000	G2	19.60	1,626	0.083
			G3	19.60	2,058	0.105
40	A1736	83061000	G3	17.38	8,980	0.517
			G2	17.39	7,058	0.406
41	A1763	83044000	G2	39.44	6,374	0.162
			G3	39.38	7,278	0.185
42	A1772	81013000	G3	42.55	2,723	0.064
			G2	42.56	2,400	0.056
43	A1774	83049000	G2	32.92	5,020	0.152
			G3	32.91	5,586	0.170
44	A1775	85056000	G2	32.78	9,963	0.304
			G3	32.77	9,446	0.288
45	A1795	80006000	G3	34.77	59,068	1.699
			G2	34.77	58,694	1.688
46	A1835	82052000	G3	17.84	6,839	0.383
			G2	17.84	5,753	0.322
		82052010	G3	15.68	6,070	0.387
			G2	15.69	5,486	0.350
47	A1851	82007000	G3	36.21	1,464	0.040
			G2	36.15	1,564	0.043
48	A1895	83033000	G2	24.34	1,333	0.055
			G3	24.34	1,762	0.072

3 SPECTRAL-IMAGING ANALYSIS

We apply our spectral-imaging deconvolution process to the observed GIS events between $1 - 9$ keV in energy [a limit imposed by the PSF images stored in the calibration databse (CALDB) at Goddard Space Flight Centre (GSFC)] using exactly the same methodology applied to the simualated datasets presented in Paper-I (*i.e.* we run the *SID* procdure on 10 randomisations of the observed events and then average the spectral-fit results obtained from all these deconvolved datasets). We also employ more conservative parameters (see details below) than applied to the simulated data in Paper-I, to yield fewer annular bins. This ensures that the results

Table 1. Observational Dataset Statistics – contd.

#	Object	Sequence Number	Inst.	Exposure (k.sec.)	Cluster Counts	Count Rate
49	A1914	84032000	G2	35.86	12,676	0.353
			G3	35.85	15,781	0.440
50	A1942	83000000	G2	34.32	2,695	0.079
			G3	34.31	3,186	0.093
51	A1995	82005000	G3	28.31	2,041	0.072
			G2	28.31	1,617	0.057
52	A2029	81023000	G2	34.06	62,198	1.826
53	A2034	84022000	G3	41.70	16,517	0.396
			G2	41.70	14,105	0.338
54	A2052	85061000	G3	42.89	40,880	0.953
			G2	42.90	35,308	0.823
55	A2063	81002000	G2	21.63	17,975	0.831
56	A2065	84054000	G3	24.22	16,757	0.692
			G2	24.29	18,372	0.756
		84054010	G2	22.78	15,222	0.668
			G3	22.75	17,031	0.748
57	A2104	84072000	G2	52.79	11,151	0.211
			G3	52.78	13,399	0.254
58	A2107	85060000	G3	28.01	13,766	0.492
			G2	28.01	13,568	0.484
59	A2142	81004000	G2	14.64	28,341	1.935
60	A2147	83074000	G2	37.09	34,801	0.938
			G3	36.94	34,953	0.946
61	A2151	83030000	G3	28.17	10,499	0.373
			G2	28.17	8,726	0.310
62	A2163	80024000	G2	31.60	18,783	0.594
			G3	31.15	18,324	0.588
63	A2199	80023000	G2	33.44	76,799	2.296
			G3	33.44	76,282	2.281
64	A2204	82045000	G2	16.05	11,723	0.731
			G3	16.05	14,290	0.891
		82045010	G2	20.07	13,280	0.662
			G3	20.07	16,741	0.834
65	A2218	80001000	G2	38.08	8,451	0.222
			G3	38.07	8,820	0.232
66	A2219	82037000	G3	35.76	12,926	0.361
			G2	35.76	10,303	0.288
67	A2255	84012000	G3	47.08	23,912	0.508
			G2	47.10	22,826	0.485
		84012010	G2	39.23	17,084	0.435
			G3	39.44	19,711	0.500
68	A2256	10004030	G3	26.53	43,010	1.621
			G2	26.53	40,018	1.508
		80002000	G3	36.44	55,265	1.517
			G2	36.45	59,364	1.629
69	A2261	84062000	G3	20.22	5,358	0.265
			G2	20.25	5,589	0.276
70	A2319	80041000	G2	14.57	36,891	2.532
			G3	14.56	44,361	3.046
		80041010	G2	13.96	38,099	2.729
			G3	13.96	35,475	2.541

Table 1. Observational Dataset Statistics – contd.

#	Object	Sequence Number	Inst.	Exposure (k.sec.)	Cluster Counts	Count Rate
71	A2390	82032000	G3	8.81	3,898	0.443
			G2	8.81	3,210	0.364
		82032010	G3	7.80	2,998	0.384
			G2	7.80	2,478	0.318
		82032020	G3	5.21	1,956	0.376
			G2	5.21	1,665	0.320
72	A2440	81033000	G3	40.00	10,324	0.258
			G2	40.01	9,859	0.246
73	A2597	83062000	G2	42.18	22,577	0.535
			G3	42.16	22,831	0.541
74	A2634	83002000	G2	41.23	16,626	0.403
			G3	41.23	17,192	0.417
75	A2657	84002000	G2	48.49	24,886	0.513
			G3	48.43	29,192	0.603
76	A2670	82049000	G2	29.16	6,527	0.224
			G3	29.15	7,264	0.249
77	A2811	84003000	G2	49.84	14,200	0.285
			G3	49.82	15,262	0.306
78	A3112	81003000	G3	36.62	29,570	0.808
			G2	36.62	26,438	0.722
79	A3158	84020000	G2	35.82	27,696	0.773
			G3	35.83	33,619	0.938
80	A3221	83048000	G2	25.01	9,615	0.384
			G3	25.02	11,067	0.442
81	A3266	83023000	G2	33.51	48,161	1.437
			G3	33.50	50,999	1.522
82	A3376	84056000	G3	22.42	10,403	0.464
			G2	22.40	11,271	0.503
83	A3391	72019000	G2	21.18	11,591	0.547
			G3	21.18	12,932	0.610
84	A3526	80032000	G2	19.36	61,758	3.190
			G3	19.36	61,773	3.191
		83026000	G2	72.31	209,227	2.893
			G3	72.31	241,614	3.341
85	A3558	82046000	G3	15.53	26,330	1.695
			G2	15.54	26,917	1.732
		83058000	G2	29.22	36,039	1.233
			G3	29.22	40,019	1.370
86	A3562	84041000	G2	20.04	12,291	0.613
			G3	20.03	13,202	0.659
87	A3571	82047000	G2	24.33	74,343	3.056
			G3	24.33	75,252	3.093
88	A3627	84005000	G2	41.47	83,424	2.011
			G3	41.44	93,158	2.248
89	A3667	83054000	G2	19.68	28,130	1.429
			G3	19.68	31,778	1.615
90	A3921	83048010	G3	19.51	8,714	0.447
			G2	19.49	7,730	0.397
91	A4059	82030000	G3	35.77	28,134	0.786
			G2	35.77	27,977	0.782
92	2A0336	82029000	G2	20.07	40,550	2.021
			G3	20.06	42,397	2.113

from the real data are less affected by systematic effects, albeit with some loss of spatial resolution.

As we are attempting to determine the spectral properties of regions of low surface-brightness it is important that we account for the contamination of the cluster data by instrumental and cosmic X-rays. This is done using the blanksky observations, contained in the CALDB at GSFC. The differences between the Galactic col-

umn density applicable for the blanksky field and each cluster are unlikely to cause significant problems because the lowest energy used in the analysis is 1 keV. (Some possible exceptions to this may occur in very high Galactic column density clusters, where we sometimes see complications in fitting cooling flow models, as discussed in Section 3). As we noted in Paper-I, we have combined the

Table 1. Observational Dataset Statistics – contd.

#	Object	Sequence Number	Inst.	Exposure (k.sec.)	Cluster Counts	Count Rate
		82040000	G2	46.16	66,679	1.445
93	AWM4	83072000	G2	51.42	10,188	0.198
			G3	51.12	12,491	0.244
94	AWM7	80036000	G2	14.95	38,107	2.549
			G3	14.95	37,574	2.513
95	CL0016	80025000	G3	32.09	1,827	0.057
			G2	32.29	1,816	0.056
		84016000	G3	58.36	3,189	0.055
			G2	58.91	3,155	0.054
96	Cygnus-A	70003000	G3	24.24	51,157	2.110
			G2	24.26	44,618	1.839
		70003010	G3	36.53	64,741	1.772
			G2	36.53	74,347	2.035
97	Klemola44	83004000	G2	55.31	45,646	0.825
			G3	55.16	53,551	0.971
98	MKW3s	80011000	G3	29.67	24,396	0.822
			G2	29.69	24,279	0.818
99	MKW4s	83008000	G2	48.32	4,704	0.097
			G3	48.33	5,602	0.116
100	MKW9	83009000	G3	46.64	3,988	0.086
			G2	46.66	3,753	0.080
101	Ophiuchus	80027000	G2	8.75	76,982	8.798
			G3	8.75	79,839	9.124
102	PKS0745-19	81016000	G2	40.67	48,774	1.199
			G3	40.67	54,352	1.336
103	SC1327	83059000	G2	30.03	14,735	0.491
			G3	29.87	15,792	0.529
104	Tri.Aus.	83060000	G2	11.85	37,459	3.162
			G3	11.85	38,543	3.253
		83060010	G2	6.95	15,877	2.283
			G3	6.95	18,521	2.666
105	Virgo	60033000	G2	16.87	134,917	7.995
			G3	16.87	137,748	8.163
106	Zw3146	80014000	G3	33.66	8,233	0.245
			G2	33.65	7,740	0.230

blanksky observations, which are divided according to COR_MIN values, so that the resulting background datafile has the same distribution of COR_MIN values as that of the cluster observation.

One important issue we had to resolve in the spectral analysis was a way to determine an automatic and objective way of selecting the sizes of the annular regions for the X-ray event extractions. In optimal circumstances one would choose a bin size which yields a constant signal-to-noise in each radial bin. However, the Maximum-Likelihood image deconvolution introduces systematic variations in regions where the surface-brightness changes relatively slowly and has less flux (*i.e.* in the outer regions of cooling flow clusters or non cooling-flow clusters). Using fixed bin-widths of size sufficient to smooth over these these systematic variations then results in a loss of spatial resolution for more distant clusters. Consequently, we have chosen a procedure which yields approximately the same number of bins in each cluster, provided the cluster is sufficiently bright, by requiring a fixed ratio of the total background-subtracted flux to be present in each annulus. Our chosen ratio of $\frac{1}{6}$th leads to a maximum of approximately five or six radial bins. If this prescription results in less than 2,000 background-subtracted counts in any annulus, then the ratio is progressively

reduced by a factor of 1.25 until this criterion is met (providing the background-subtracted number of counts does not fall below a hard limit of 1,000 counts)[§]. As will be seen, this procedure gives reasonable spatial resolution for distant clusters, and does not over-sample bright ones. The distribution of the number of annuli for the results are as follows: 1 bin – 8 clusters; 2 bins – 5 clusters; 3 bins – 8 clusters; 4 bins – 17 clusters; 5 bins – 67 clusters; 6 bins – 1 cluster. Thus, 93 percent of the clusters in the sample have more than a single annulus in their combined radial profiles, 80 percent have 4 or more, and 64 percent have more than 5 annuli.

Having obtained annular spectra for each cluster, we then fit what we consider to be the simplest physically-plausible spectral model to determine the radial variations in the properties of the intracluster gas: a single thermal emission component (MEKAL: Mewe, Gronenschild, & van den Oord 1985; Mewe, Lemen, & van den Oord 1986), modified by foreground absorption (Morrison & McCammon 1983) according to the Galactic column density (Stark et al. 1992). This model is applied to data between 1 and $9\,\mathrm{keV}$[¶]. In all the deconvolved-data spectral fits we include 10 percent systematic errors to account for some uncertainty in the accuracy of the *ASCA* PSF. (This produces χ^2_ν values which are slightly less than unity compared to those fits without the 10 percent systematics – which are generally around one.)

We also calculate an average broad-beam temperature for each cluster using the non-deconvolved data, because we do not require any spatial information. This has the advantage that we can cross-check our deconvolved results against the 'unprocessed' data (see the plots in Appendix B which show these average temperatures overplotted on the deconvolved profiles). As well as the single-phase model we also fit a model which includes emission from a cooling flow. This latter model introduces only one additional free parameter, the mass deposition rate (*i.e.* normalisation), because the other parameters such as the temperature from which the gas cools and the metallicity are tied to that of the single phase component. By fitting the data from both GIS detectors simultaneously we obtain the single-phase model parameter constraints, as indicated in Table A1, and cooling flow model parameters, as listed in A2. (Note, the 10 percent systematics are not included on the broad-band fits because these are not derived from the deconvolved datasets.)

Although a cooling flow spectrum has been fitted to all the data, this does not mean that it is an applicable model for all datasets. Section includes a description of the values in Tables A1 and A2 which should be compared to determine whether the additional parameter in the cooling flow model provides a statistically

---

[§] Note, in the simulations tests in Paper-I the nominal fraction of the total number of background-subtracted counts per annulus was set to 0.1, the soft-limit on the minimum number of counts in an annulus was 1,000 and the hard-limit was 500 counts. In this analysis these parameters are: 0.167, 2,000 and 1,000 counts, respectively.

[¶] The GIS2 data which come from observations where the GIS3 data were contaminated by the analogue-digital conversion problem were fitted $2.5 - 9\,\mathrm{keV}$. This resulted in better behaviour for the temperature profiles, especially in A2029. Note, the GIS3 results for A773 and A854 were also neglected as these gave implausibly high temperatures in the outer regions.
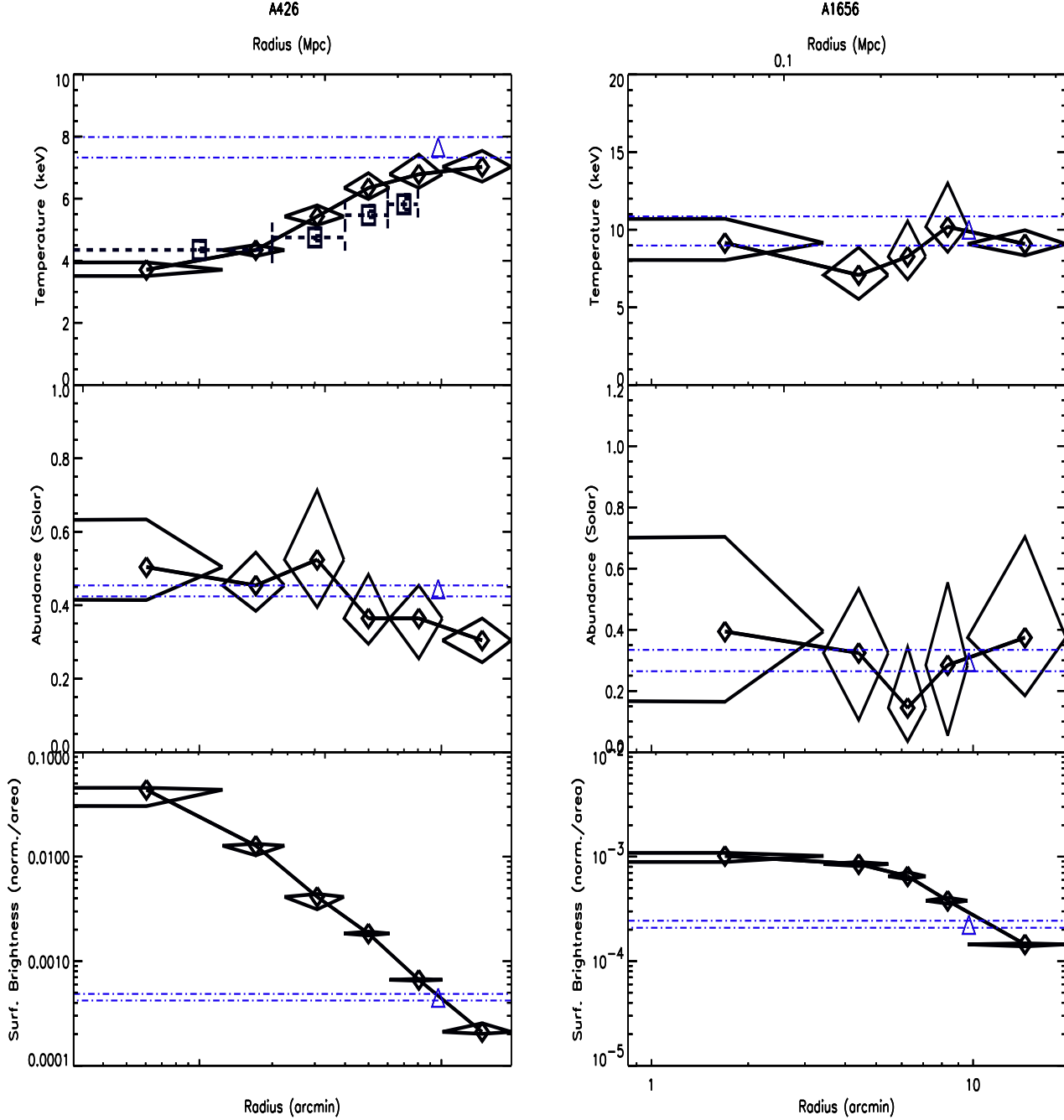
Figure 1. This figure presents example of the spectral analysis results on a cooling flow cluster, A426 (Perseus), and non cooling-flow A1656 (Coma Berenices). The heavy solid-lines are the average of the spectral fit results for a single-phase plasma applied to the GIS2 and GIS3 deconvolution results. The single triangle data-points, with error-bars which span the whole radius range, are the the cooling-flow spectral fits to the non-deconvolved data. The additional temperature profile (square symbols) for A426 is from Beppo-SAX (see the end of Section 3 for the reference).

significant improvement over the single-phase model. We find that in approximately half our sample the decrease in χ^2_ν, due to the addition of this extra cooling flow component, is significant at more than 90 percent (the significance at 68 percent confidence may be judged from the errors on the mass-deposition rate in Table A2).

In Section 4 we discuss particular examples of the results from

the deconvolution analysis and quantify the overall isothermality of our cluster sample. Firstly, we discuss individual graphical examples of the results for five clusters which show the deconvolved radial temperature, metallicity, and model normalisation (divided by the region area) profiles for each GIS detector. We also overplot the broad-beam average results from the non-deconvolved data which indicate the temperature obtained from the cooling flow spectral

model. Similar graphical presentations, excluding the emissivity profiles, for the results for the whole sample of 106 clusters are given in Appendix B. Broad-beam temperatures (from original data) are also overplotted for the cooling flow model – this has the advantage that it shows the 'ambient' cluster temperature, *i.e.* the effect of the cooling flow on the cluster's temperature is corrected for.

For the clusters where temperature profiles are published by Markevitch et al. (and references within) we have also overplotted their data (after converting their 90 percent uncertainties to our 1-σ limits) on the temperature profiles. Some results (including some abundance profiles) from other satellites such as *ROSAT* (A478 – Allen et al. 1993; A3526 – Allen & Fabian 1994; A1795 – Briel & Henry 1996) and Beppo-SAX (A426 – Molendi 1998; A2319 – Molendi et al. 1999; Virgo – D'Acri, Grandi, & Molendi 1998) are also plotted.

3.0.1 *Creating Averaged Radial Profiles From Many Datasets*

The radial profiles which we present in the various figures, are created from the averaging of many datasets. These come from: (i) our 10 Monte-Carlo runs which we have employed to average the systematic variations in single-runs of the *SID* procedure; (ii) the observations from the two GIS detectors, and (iii) occasionally multiple observations of a cluster.

To perform this 2-d averaging, we create a grid which covers the ranges of values in both dimensions. Then, for example, in an temperature versus radius plot we take each temperature data point, and its associated errors, and create a Gaussian distribution to describe the function in the y-axis direction. Similarly, for the radial data we create an x-axis function using a triangular function to represent the emission-weighted radius (an alternative would be to use a top-hat function but this weights all positions within the radial extent of the bin equally). Then we combine these x- and y-functions and construct a 2-d probability distribution (normalised to unity over its entirety). This is then placed at the appropriate position in our 2-d grid. This process is repeated for all data points to build up an image of the total 2-d probability distribution function. We then simply sample this grid on any chosen scale to obtain our averaged radial profile. We chose a sampling which yields approximately the same binning as the best of the original datasets in each cluster.
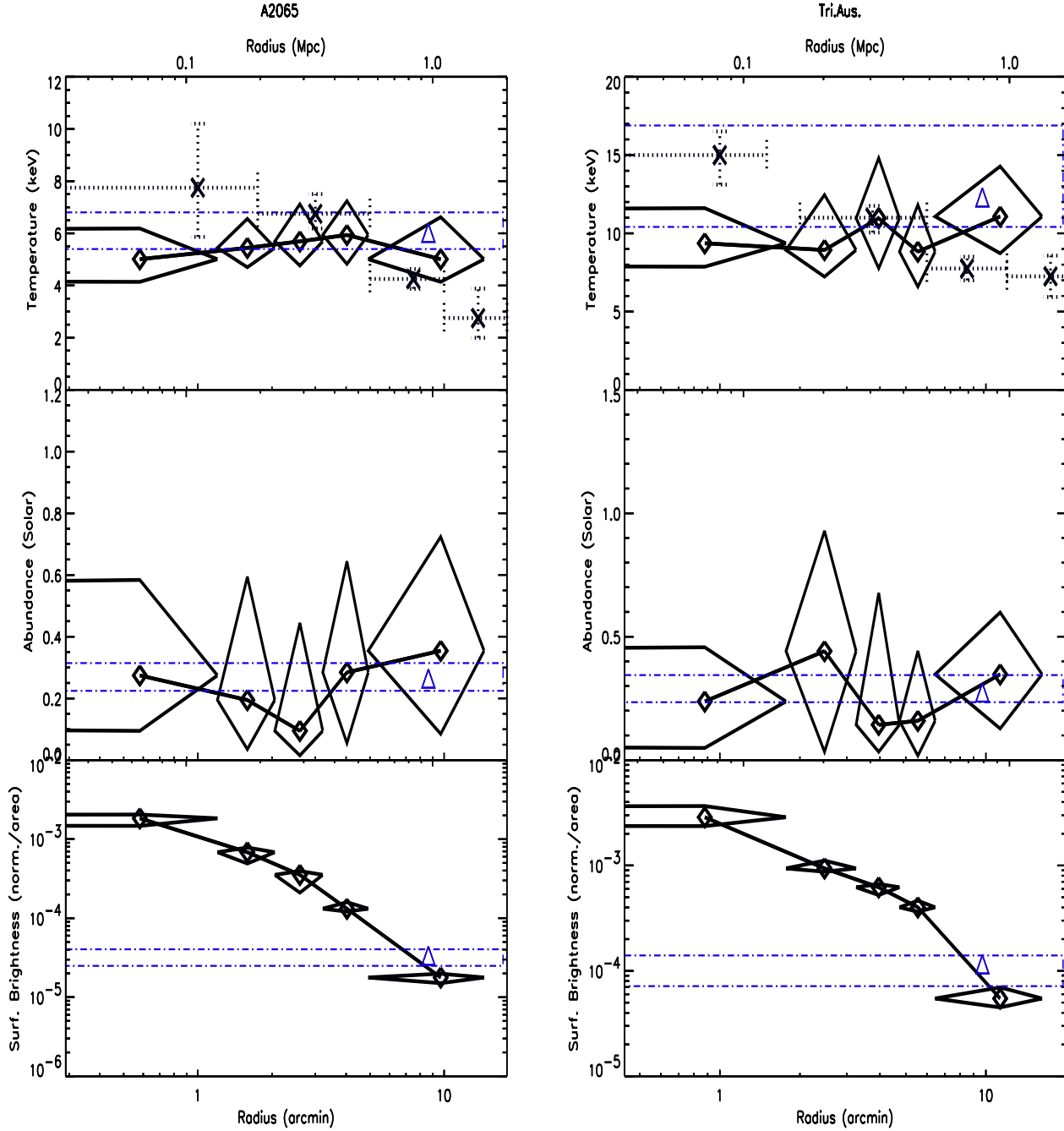
4 RESULTS

4.1 Discussion Of Individual Examples

Fig. 1 shows the radial profiles and broad-beam averages for the Perseus (*i.e.* A426 – the brightest X-ray cluster) and Coma Berenices (A1656) clusters, highlighting the difference between classic examples of cooling and non cooling-flow clusters, respectively. The temperature decline due to the cooling flow in A426 is clearly detected, and there is some evidence for an abundance gradient. In comparison, A1656 presents an isothermal temperature profile with a flat abundance profile, and has a less sharply peaked emissivity profile.
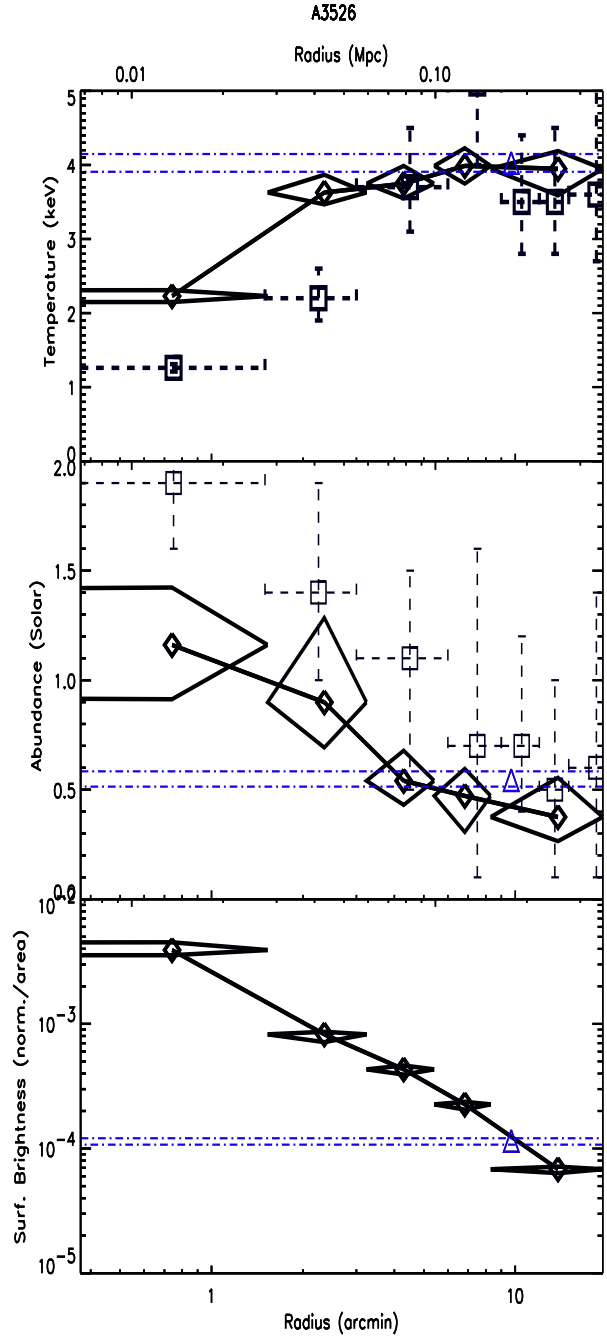
Figure 2. This figure shows the detailed results for A3526 (Centaurus cluster). Additional temperature and abundance profiles from *ROSAT* are shown with square symbols (see the end of Section 3 for the reference).

Fig. 2 presents a direct comparison of our results with those from *ROSAT* data by Allen & Fabian (1994) for the Centaurus cluster (A3526). Although our *ASCA* determination of the temperature profile exhibits a slightly shallower decline in the core of the Centaurus cluster, and slightly lower overall metallicity when compared with the *ROSAT* results, the general consistency between these results is good. [We also note that the *ROSAT* results were

Figure 3. This figure shows examples of the discrepancy between our results and those presented by *MFSV* for the A2065 and Triangulum Australis clusters. Our results indicate isothermal temperature profiles, contrary to the *MFSV* results which show temperature declines (which are shown by the cross symbols with dotted error-bars).

obtained fitting a Raymond, Cox, & Smith (1976) plasma model, while we have used the MEKAL model used in this analysis. Thus, the differences, especially in the abundance profiles, will partially be due to the plamsa codes and the abundance definitions, and also the lack of excess absorption in our model.] As the *ROSAT* data do not require the spectral-imaging deconvolution, the fact the general trends are in agreement indicates that our method can recover the intrinsic radial properties of the intracluster gas. Perhaps the most

noticeable feature is the strong abundance gradient, confirming the *ROSAT* detection by Allen & Fabian (1994) and the early *ASCA* analysis by Fukazawa et al. (1994).

The results for Triangulum Australis and A2065 clusters illustrate particular examples of the discrepancy between some of our results and those of *MFSV*. It is clear that our profiles appear to be isothermal while the *MFSV* results show their characteristc temper-

ature decline. This is typical for most of the clusters common to both analyses (see Appendix B). There are notable examples where our results show good agreement at all radii, but these tend to be those clusters where *MFSV* find relatively flat temperature profiles (*e.g.* AWM7). Overall it appears that we find that our temperature profiles are flatter (see two particular examples in Fig. 3 and others in Appendix B); at intermediate radii the agreement is often good but our temperature determinations are generally cooler in the core and hotter in the outermost regions. Only in a handful of clusters (*e.g.* A1553, A1689, A1774, A2034, A2218) do we see significant systematic declines with increasing radius, and many of these are clusters with poorer data which may suffer from uncertainties in background subtraction.

In our final example we plot our results against those of Markevitch et al., and those from the recent Beppo-SAX result on A2319 by Molendi et al. (1999). Our temperature profile is relatively flat (the slight increase with radius is probably not very significant given the relatively large uncertainties), and it agrees fairly well with the SAX data which have much smaller errors. Clearly the SAX data shows that this cluster has an isothermal temperature profile. For the Markevitch et al. data, the outer point in the temperature profile is low compared to their inner values, and is typical of their their temperature decline trend. As an aside, our *SID* abundance profile also agrees well with the SAX result.

The most significant apparent departures that we see from isothermality are the declines in the single-phase temperature within the core regions of some cooling flow clusters – see for example the Figs. 1(a) and 2 for the Perseus and Centaurus clusters respectively. Without any extra information we would be unable to claim that the underlying ambient temperature for these clusters is isothermal. However, when we fit the cooling flow emission model to the broad-band spectra (*i.e.* data which have not been deconvolved) we find that the 'representative' temperature of the model increases to a consistent level with the spatially-resoved (*i.e.* deconvolved) single-phase temperature found in the outer regions of the cluster – see Fig. 1. In other words, when we correct for the cooling flow 'contamination' we find that the mean temperature is the same for the whole cluster as it is for the outer regions.

A similar result is seen in most of the other clusters where a cooling flow causes a significant drop in the average single-phase temperature profile, as can be seen in a comparison for of the average single-phase temperature and the cooling flow corrected temperature in Tables A1 and A2, and the plots in Appendix B. (Notable cooling flow exceptions are: A478, PKS0745 and 2A0336, but in these cases the agreement can be obtained by allowing excess absorption on the cooling flow component of the spectrum in the core of the cluster – which is not unreasonable given that these clusters have high column densities which can affect the spectrum above the 1 keV lower limit.)

4.2 Quantifying The Ubiquity Of Cluster Isothermality

From our *SID* analysis it is visually apparent that the clusters in our sample are generally consistent with isothermality. Even in cooling flow clusters where the single-phase temperature exhibits a decline on the core temperature, a broad-spatial temperature determination, corrected for the cooling flow effect, shows that the 'ambient' tem-
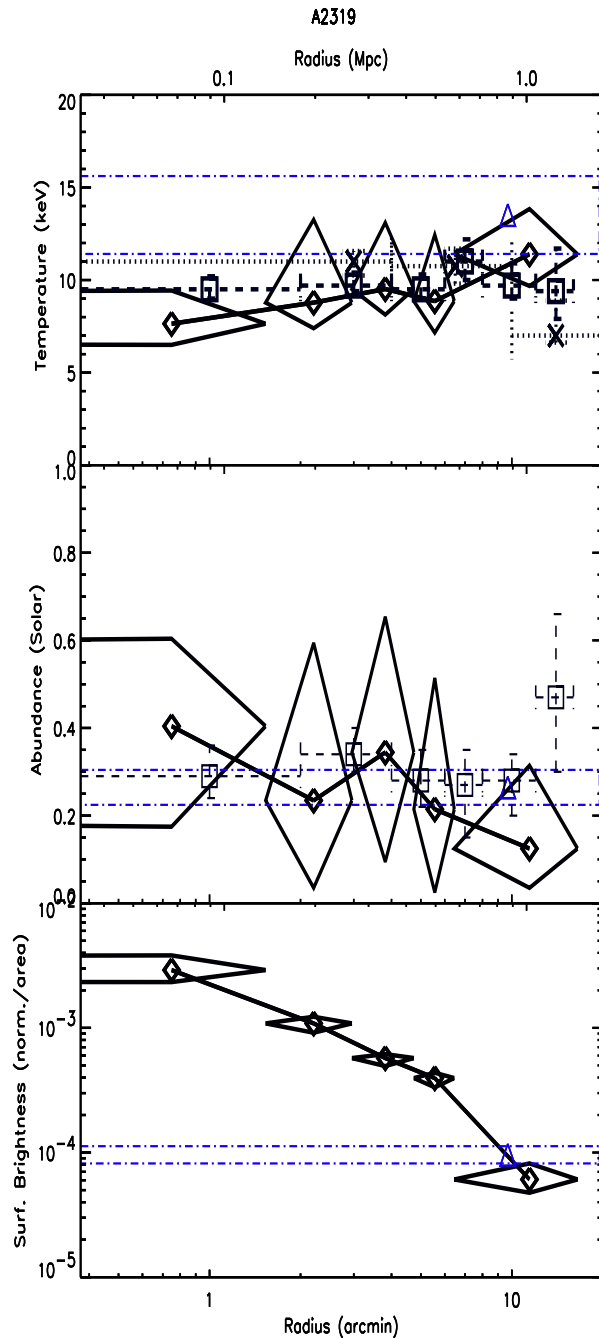
Figure 4. This figure compares the results from our *SID* analysis (solid line, triangle symbols), those of Markevitch et al. (dotted line, 3 cross symbols for temperature profile), and the Beppo-SAX results from Molendi et al. (dashed line, 6 square symbols for temperature and abundance profiles).

perature in the core is the same as in the outer regions; and therefore that these cooling flow clusters are also, essentially, isothermal.

We have attempted to quantify the significance of the isothermality in our sample by fitting each cluster's (having more than a single annular bin) average temperature profile with a simple power-law function. The distribution of the best-fit slopes and the

significance of these deviations from a flat profile (zero slope) are shown in Fig. 5(a). The cumulative distribution illustrates that approximately 90 percent of the clusters in our sample are consistent with having isothermal temperature profiles, within the 3-σ confidence limit (and no account has been made here for the obvious core temperature drop in some of the cooling flow clusters). Admittedly, the errrors on the temperature profiles are large, but the sample's slopes are distributed fairly symmetrically around a value of zero (*i.e.* a flat profile).

As we find that our sample is essentially consistent with a population of isothermal clusters, we are left with the question as to the source of the discrepancy between our method and that of *MFSV*. As we noted in Paper-I, their method uses the *ROSAT* emissivity profile over $0.2 - 2\,\mathrm{keV}$ while their *ASCA* analysis is over $2 - 10\,\mathrm{keV}$. If the emissivity profile is significantly different between these two energy bands then this procedure will yield incorrect results. If the *MFSV* results are biased by such an effect the we would expect hotter clusters to be more severely affected. We can test to see whether such systematic effect exists in the *MFSV* results by plotting the slope of their temperature profiles against the average temperature. Fig. 6 shows that their hotter clusters do have, on average, steeper temperature declines. Although this weak trend could be physical in nature, it is also possible that it is due to the assumption used in the *MFSV* method.

4.3   Abundance Gradients

From our two example cooling flow clusters, especially the Centaurus cluster (A3526), we see that their abundance profiles decline systematically with radius. (Note, metallicity determinations are less affected by the scattering problem as the abundances are measured with respect to the local continuum.) Some other clusters which show a decline are: A85*, A478*, A496*, A426*, A576, A586, A990*, A1413, A2029, A2034*, A2052, A2199*, A3526*, A0459, Cygnus-A*, Klemola 44*, PKS-0745*, and Virgo*. Those clusters with the superscripted asterix are those where we find that the cluster has a significant cooling flow, on the basis of the mass-deposition rate values in Table A2. Clearly most of these are cooling flow clusters.

This list of objects was constructed from a visual inspection of the plots in Appendix B. For a more subjective investigation of the prevalence of abundance gradients in the overall sample, we have fitted all the metalliticy profiles with a power-law in the same manner as we fitted the temperature profiles in Section 4.2. Fig. 5(b) shows average abundance-profile slope, for those clusters with two or more annuli, is approximately -0.2. The uncertainties on these fits is such that 90 percent of this sample are consistent with a flat profile at only 1.5σ, and so this deviation is not statistically significant. This does not mean that there is not a decline in a sub-class of clusters, such as cooling flows, as this question is not addressed by our statisical test. In fact, our impression, from our quick visual inspection of the radial profiles for cooling flows, would support the hypothesis that abundance gradients are more prevalent in cooling flow clusters. However, this clearly requires further study.

5   CONCLUSIONS

We have determined the projected radial temperature, metallicity and emissivity profiles for 106 clusters of galaxies, which have been obtained using our spectral-imaging deconvolution procedure. We present plots of the temperature and abundance profiles for all these clusters (93 percent of the sample have two or more annular bins).

We developed this method was developed to correct for the energy and position dependent point-spread function of the *ASCA* setellite, which would otherwise confuse any spatially-resolved spectral analysis of extended sources. Our primary goal is to use this method to extract cluster temperature profiles from *ASCA* data in order that we place constraints on the mass properties of a large number of clusters (Paper-III, in preparation).

In this paper we concentrate on investigating whether we find the same ubiquitous trend for declining temperature profiles which Markevitch et al. (1998) find from their analysis of 30 galaxy clusters. If their result is correct, it is of fundamental importance because temperature profiles have implications for cluster properties and cosmology. For example, cluster baryon fraction estimates will increase due to the smaller total mass implied by declining temperature profiles as compared to isothermality. This exacerbates the discrepancy between primordial nucleosythesis constraints and clusters baryon fractions (*e.g.* White et al. 1993; White & Fabian 1995), and implies smaller values for Cosmological Density parameter.

However, we personally have reservations about the ubiquity and steepness of these temperature declines. The average polytropic index in their sample is $\gamma = 1.24^{+0.20}_{-0.12}$ (*i.e.* $\Gamma \sim 4/3$), which is statistcally consistent (at ~ 2-σ) with the convective instability boundary at $\Gamma = 5/3$. Given that this near convective instability could be due to merger events, this would be inconsistent with the proportion of cooling flows which they find in their sample (60 percent), because the cooling flow process would be destroyed in a strong merger event (*i.e.* see Buote & Tsai and Buote).

Further doubts have been raised by Irwin, Bregman, & Evrard (1998). They have compared the results from Markevitch et al. with other analyses (*i.e.* Ikebe et al. 1997; Fujita et al. 1996; Ezawa et al. 1997; Ohashi et al. 1997) – all of which seem to show isothermal profiles where Markevitch et al. find a temperature decline. Irwin et al. also present their own analysis of *ROSAT* X-ray 'colour' profiles from which they conclude that the clusters are consistent with isothermality, excluding core regions which may be contaminated by the effects of cooling flows.

With our 106 clusters, which includes all those in the Markevitch et al. sample, we find that our spectral-imaging deconvolution procedure generally yields isothermal temperature profiles. In only a handful of clusters do we find any obvious systematic decline (although the addition of a cooling flow component improves the spectral fits in approximately 50 percent of the sample). The significance of our result is such that when we fit power-law functions to each of our cluster temperature profiles, approximately 90 percent are consistent with isothermality at the 3-σ limit. For those clusters common to both samples we find that although there is often reasonable agreement at intermediate radii, our core temperatures are cooler and our outer temperatures are hotter. In strong cooling flow clusters, where we detect a drop in the single-phase temperature of the gas due to the effect of cooling, we also find that correcting for
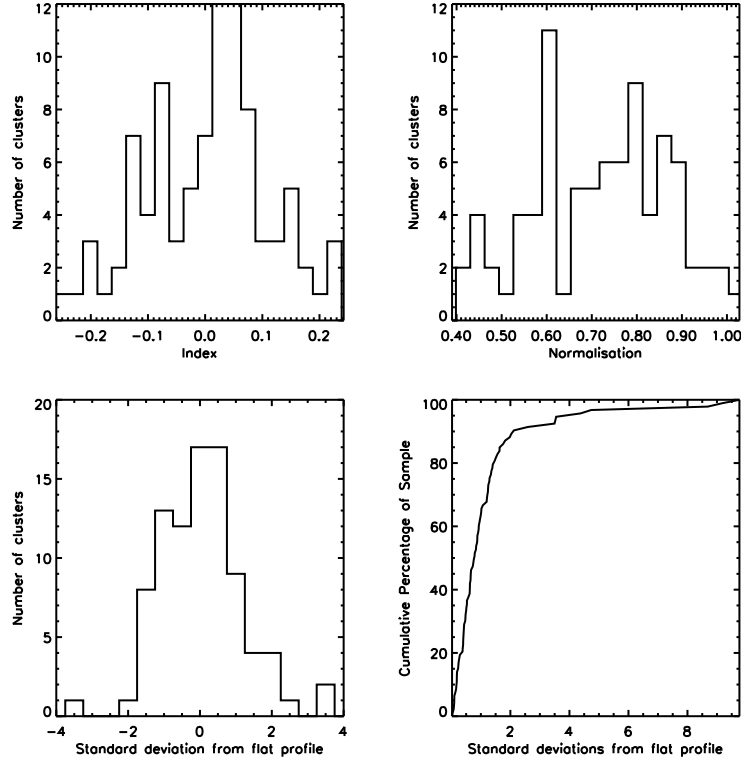
(a) Temperature Profile Fit Parameters
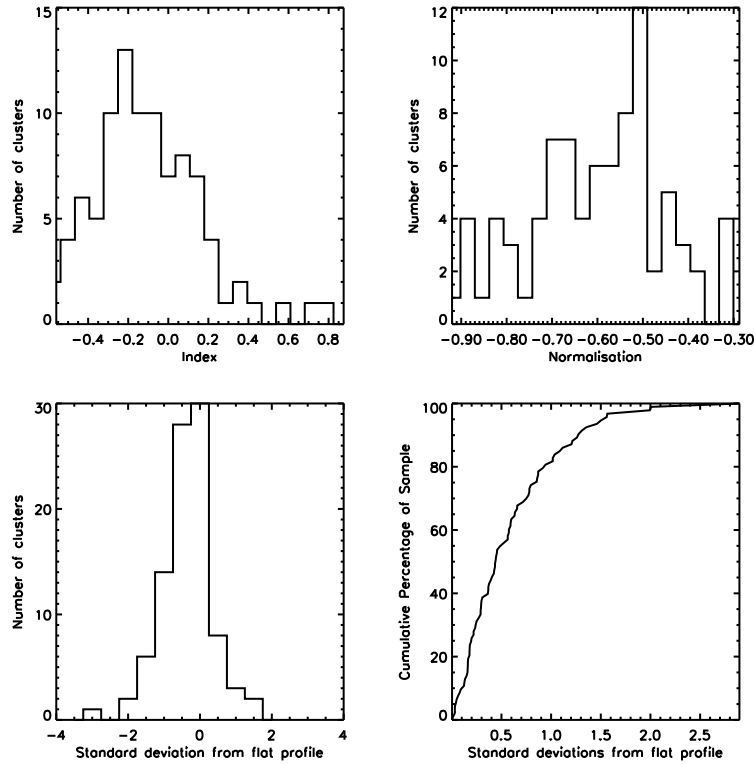
(b) Metallicity Profile Fit Parameters

Figure 5. This figure summarises the slopes of the (a) temperature and (b) abundance profiles of all the clusters in our sample. For each group of four plots we show the distribution of slopes and normalisation of the power-law model fitted to each cluster's profile; the number of standard-deviations of the fitted slope from a flat profile (*i.e.* isothermality for the temperature profiles); and finally the cumulative distribution of these number of standard-deviations. From figure (a) we conclude that the sample is on average isothermal, and from figure (b) that there is a general abundance gradients in which metallicity decreases with radius, but that it is not statistically significant for the sample as a whole.
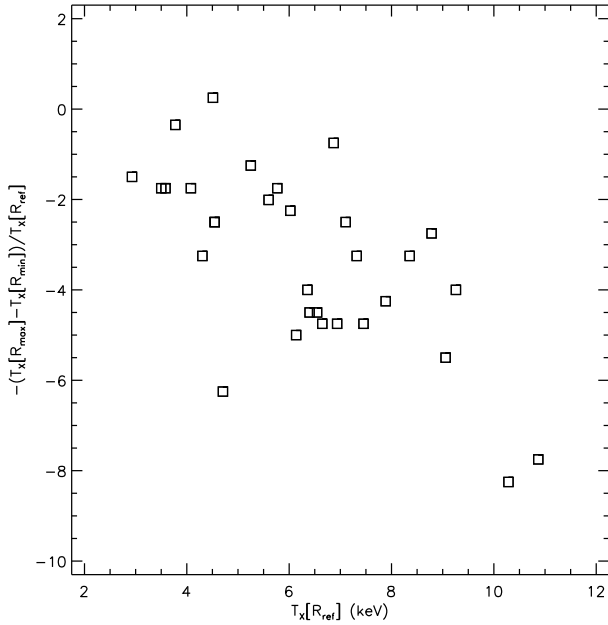
Figure 6. This figure presents data from Markevitch et al. to investigate the possible systematic bias discussed in Section 4.2. The ordinate data shows the normalised temperature decline (*i.e.* the difference in temperature between the inner and outermost radii, normalised by the inner temperature) plotted against the weighted-average temperature. The Pearson rank correlation test indicates that there is a marginal correlation in the data (1-σ) deviation from the null hypothesis; the deviation is 3-σ when the inner temperature is used as the abscissa). From this plot we see that, in the Markevitch et al. sample, there is a tendency for hotter clusters to have larger (normalised) declines than the cooler clusters.

this effect indicates that the 'ambient' core temperature is consistent with the outer regions of the cluster. This indicates that even in cooling flows, the underlying temperature profile is consistent with being isothermal.

Our procedure also allows some constraints to be placed on the abundance profiles, although the systematic uncertainties are much larger than in the temperature profiles. There are examples of a clear metallicity enhancements within the core regions of some clusters, such as that for the Centaurus cluster – cofirmining the previous detections by Allen & Fabian (1994); and Fukazawa et al. (1994)]. While this effect is visually most noticeable in cooling flow clusters, the decline (a power-law slope of -0.2) is not statistically significant (because of the uncertainties) in the sample as a whole.

In Paper-III White (1999) we present the constraints on gravtiational masses, baryon fractions and mass-profile model parameters, which we have been able to obtain for a subsample of the clusters in this paper.

6 ACKNOWLEDGEMENTS

REFERENCES

Allen S.W., Fabian A.C., 1994, MNRAS, 269, 409

Allen S.W., Fabian A.C., Johnstone R.M., White D.A., Daines S.J., Edge A.C., Stewart G.C., 1993, MNRAS, 262, 901

Briel U.G., Henry J.P., 1996, ApJ, 472, 131

Buote D.A., 1998, 293, 381

Buote D.A., Tsai J.C., 1996, ApJ, 458, 27

D'Acri F., Grandi S. De, Molendi S. 1998, astro-ph/9802070

Edge A.C., Stewart G.C., Fabian A.C., Arnaud K.A., 1990, MNRAS, 245, 559

Ettori S., Fabian A.C.MNRAS, submitted

Ezawa H., Fukazawa Y., Makashima K., Ohashi T., Takahara T., Xu H., Yamasaki N.Y., 1997, ApJ, 490, L36

Fujita Y., Koyama K., Tsuru T., Matsumoto H., 1996, PASJ, 48, 191

Fukazawa Y., Ohashi T., Fabian A.C., Canizares C.R., Ikebe Y., Makashima K., Mushotzky R.F., Yamashita K., 1994, PASJ, 46, L55

Ikebe Y. et al., 1997, ApJ, 481, 660

Irwin J.A., Bregman J.N., Evrard A.E., 1998, ApJ, Vol. N/A, submitted

Markevitch M., Forman W.R., Sarazin C.L., Vikhlinin A., 1998, ApJ, in press, astro–ph/9711289v2

Mewe R., Gronenschild E.H.B.M., Oord van den G.H.J., 1985, A&A, 62, 197

Mewe R., Lemen J.R., Oord van den G.H.J., 1986, A&A, 65, 511

Molendi S.

Molendi S., Grandi S. De, Fusco-Femiano R., Colafrancesco S., Fiore F., Nesci R., Tamburelli F., 1999, ApJ, in press, astro–ph/9909228

Morrison R., McCammon D., 1983, ApJ, 270, 119

Ohashi T., Honda H., Ezawa H., Kikuchi K., 1997, in Makino F., Mitsuda K., eds, X-Ray Imaging and Spectroscopy of Cosmic Hot Plasmas. Universal Academy Press Inc., Tokyo, Japan, p. 49

Raymond J.C., Cox D.P., Smith B.W., 1976, ApJ, 204, 290

Stark A.A., Gammie C.F., Wilson R.W., Bally J., Linke R.A., Heiles C., Hurwitz M., 1992, ApJS, 79, 77

Takahashi T., Markevitch M., Fukazawa Y., Ikebe Y., Ishisaki Y.,

Kikuchi K., Makashima K., Tawara Y., 1995, in ASCA Newsletter, (NASA/GSFC), Volume 3

Walker T.P., Steigman G., Schramm D.N., Olive K.A., Kang Ho-Shik, 1991, ApJ, 376, 51

White D.A., 1999, MNRAS, in prep., (Paper–III)

White D.A., Buote D.A., 1999, MNRAS, accepted, (Paper–I)

White D.A., Fabian A.C., 1995, MNRAS, 273, 72

White D.A., Fabian A.C., Johnstone R.M., Mushotzky R.F., Arnaud K.A., 1991, MNRAS, 252, 72

White S.D.M., Navarro J.F., Evrard A.E., Frenk C.S., 1993, Nat, 366, 429

provides an improvement in the spectral fit at more than 90 percent significance.

APPENDIX A: TABULAR RESULTS

Tables A1 and A2 present the results of broad-band spectral analysis on the (non-deconvolved) original *ASCA* data. The GIS2 and GIS3 data in each observation have been fitted simultaneously over the $1 - 9\,\mathrm{keV}$ energy band. Table A1 shows the best-fit spectral parameters resulting from fitting a single thermal-emission component (XSPEC's MEKAL model), while Table A2 gives the results for a cooling flow model (see Section 3 for details). The MEKAL model has three free parameters: temperature, abundance and normalisation. The cooling flow model only has one more additional parameter: the mass-deposition rate (*i.e.* normalisation).

All parameters uncertainties are quoted as 1-σ standard deviations. For clusters with more than one observation we have indicated the weighted-average of the parameters determined from these multiple observation constraints.

Note, the central regions of Cygnus-A appear to be contaminated by a strong AGN. Although this has been removed in the temperature profile plots in Appendix B, no correction has been applied to these broad-band fits and so these fits may be affected by the AGN contribution – note the exceptionally large temperatures in the cooling flow model.

The first seven columns headers in each table indicate: 'Object' – cluster name; 'Seq. Num.' – *ASCA* observation sequence number; 'Inst.' – instrument used in the fit; 'A_{out} ($'$)' – outer radius of fitted region in arcminutes; z – cluster redshift; R_{out} (Mpc) – outer metric radius of fitted region (for $H_0 = 50\ \mathrm{km\,s^{-1}\ Mpc^{-1}}$, $q_0 = 0.5$ cosmology); $N_{\mathrm{H}}/10^{20}$ ($\mathrm{cm^{-2}}$) – column density normalised to $10^{20}\,\mathrm{cm^{-2}}$. For the single thermal component fits the additional column headers are: T_{X} (keV) – best fit temperature; Z ($\odot$) – metallicity as a fraction of Solar; $Norm.$ ($10^{-14}/(4\pi D_L^2 \int n_e\, n_p\, dV)$); χ_ν^2 – goodness-of-fit (for 3 free parameters in the single-phase model and 4 in the cooling flow model); and N_{PI} – the number of PI channels.

For the cooling flow data we present $\dot{M}$ ($\mathrm{M_\odot\,yr^{-1}}$) – the normalisation of the additional cooling flow spectral component. We have used the F-test to calculate the χ_ν^2 value which would be required for a 90 percent significant improvements in the the spectral fit obtained by including the cooling flow component. This value is given in the final column of Table A1, and should be compared with the value in the penultimate column of Table A2. If the latter value falls below the former then the cooling flow component

Table A1. Broad-Band Single-Phase Plasma Fit Results

Object	Seq. Num.	Inst.	A_{out} (')	z	R_{out} (Mpc)	$N_H/10^{20}$ (cm^{-2})	T_X (keV)	Z (⊙)	$Norm.$ ($\frac{10^{-14}}{4\pi D_L^2}\int n_e n_H dV$)	χ^2_ν	N_{PI}	$\chi^2_{\nu,\text{reqd.}}$ for CF mod.
A85	81024000	G2G3	19.4	0.0521	1.61	3.01	$5.94^{+0.10}_{-0.07}$	$0.38^{+0.02}_{-0.02}$	$0.101^{+0.000616}_{-0.000595}$	1.0765	1068	1.0765
	81024010	G2G3	19.4		1.61		$5.89^{+0.14}_{-0.11}$	$0.38^{+0.03}_{-0.03}$	$0.0992^{+0.000878}_{-0.000873}$	0.9710	836	0.9709
	Combined						5.92 ± 0.11	0.38 ± 0.03	0.100 ± 0.000740			
A119	83045000	G2G3	19.4	0.0443	1.39	3.45	$5.62^{+0.12}_{-0.12}$	$0.28^{+0.04}_{-0.03}$	$0.0484^{+0.000470}_{-0.000466}$	1.1023	907	1.1022
A262	81031000	G2G3	19.4	0.0163	0.54	5.33	$2.21^{+0.03}_{-0.03}$	$0.32^{+0.04}_{-0.04}$	$0.0700^{+0.00198}_{-0.00192}$	1.1449	646	1.1447
A370	80010000	G2G3	7.9	0.3730	2.94	3.02	$5.70^{+0.64}_{-0.55}$	$0.52^{+0.18}_{-0.16}$	$0.00402^{+0.000193}_{-0.000188}$	0.9032	242	0.9025
A399	82008000	G2G3	19.4	0.0715	2.14	17.10	$6.80^{+0.17}_{-0.17}$	$0.30^{+0.03}_{-0.03}$	$0.0510^{+0.000463}_{-0.000464}$	0.9817	911	0.9816
A400	83037000	G2G3	19.4	0.0238	0.77	8.82	$2.26^{+0.04}_{-0.04}$	$0.32^{+0.06}_{-0.05}$	$0.0282^{+0.000999}_{-0.000965}$	1.0870	754	1.0868
A401	82010000	G2G3	19.4	0.0748	2.23	11.10	$8.68^{+0.17}_{-0.17}$	$0.27^{+0.03}_{-0.03}$	$0.0832^{+0.000491}_{-0.000491}$	1.0519	1091	1.0519
A426	80007000	G2G3	19.4	0.0179	0.59	14.51	$5.28^{+0.03}_{-0.03}$	$0.45^{+0.01}_{-0.01}$	$0.973^{+0.00276}_{-0.00271}$	1.3946	1272	1.3945
A478	81015000	G2	18.4	0.0881	2.44	30.00	$6.58^{+0.26}_{-0.25}$	$0.31^{+0.03}_{-0.03}$	$0.106^{+0.00193}_{-0.00183}$	0.9422	415	0.9418
A496	80003000	G2G3	19.4	0.0330	1.05	4.41	$4.08^{+0.04}_{-0.04}$	$0.40^{+0.02}_{-0.02}$	$0.105^{+0.000709}_{-0.000684}$	1.0320	1063	1.0319
A521	84071000	G2G3	13.3	0.2533	3.95	5.81	$5.89^{+0.42}_{-0.34}$	$0.29^{+0.09}_{-0.08}$	$0.00989^{+0.000253}_{-0.000244}$	0.9405	506	0.9403
A539	83003000	G2G3	17.9	0.0288	0.86	13.30	$2.89^{+0.05}_{-0.05}$	$0.29^{+0.05}_{-0.05}$	$0.0393^{+0.000830}_{-0.000814}$	1.0235	707	1.0234
A548	84034000	G2G3	18.2	0.0415	1.23	2.04	$3.10^{+0.10}_{-0.10}$	$0.34^{+0.09}_{-0.08}$	$0.0192^{+0.000677}_{-0.000663}$	0.9550	547	0.9548
A576	84001000	G2G3	17.9	0.0381	1.11	5.65	$4.02^{+0.07}_{-0.07}$	$0.34^{+0.04}_{-0.04}$	$0.0359^{+0.000433}_{-0.000429}$	1.0806	885	1.0805
A586	81009010	G2	11.3	0.1710	2.55	5.72	$6.06^{+0.64}_{-0.52}$	$0.21^{+0.13}_{-0.12}$	$0.0131^{+0.000486}_{-0.000469}$	1.1165	156	1.1148
A611	84063000	G2G3	8.6	0.2880	2.77	4.99	$6.85^{+0.48}_{-0.46}$	$0.21^{+0.09}_{-0.08}$	$0.00549^{+0.000135}_{-0.000133}$	0.8706	428	0.8703
A644	83022000	G2G3	17.7	0.0704	1.93	7.32	$7.47^{+0.12}_{-0.10}$	$0.33^{+0.02}_{-0.02}$	$0.0639^{+0.000343}_{-0.000343}$	1.0633	1124	1.0632
A665	80035000	G2G3	12.8	0.1816	3.02	4.21	$7.73^{+0.41}_{-0.35}$	$0.29^{+0.06}_{-0.06}$	$0.0178^{+0.000253}_{-0.000253}$	1.0890	623	1.0888
A697	84031000	G2G3	13.0	0.2820	4.13	3.24	$8.60^{+0.50}_{-0.49}$	$0.29^{+0.07}_{-0.07}$	$0.0126^{+0.000213}_{-0.000213}$	1.0798	664	1.0797
A754	82057000	G2G3	19.4	0.0542	1.67	4.74	$9.83^{+0.27}_{-0.27}$	$0.28^{+0.03}_{-0.03}$	$0.106^{+0.000697}_{-0.000666}$	1.0977	1038	1.0976
A773	82001000	G2G3	13.8	0.1970	3.46	1.44	$8.63^{+0.68}_{-0.67}$	$0.10^{+0.09}_{-0.09}$	$0.0107^{+0.000224}_{-0.000225}$	1.0172	529	1.0170
A780	80015000	G2G3	17.2	0.0522	1.43	4.80	$3.56^{+0.05}_{-0.06}$	$0.34^{+0.04}_{-0.04}$	$0.0661^{+0.000902}_{-0.000893}$	1.1230	690	1.1228
A854	83006000	G2G3	11.1	0.2069	2.88	3.12	$6.07^{+0.58}_{-0.39}$	$0.09^{+0.10}_{-0.09}$	$0.00588^{+0.000168}_{-0.000166}$	0.9812	418	0.9809
A963	80000000	G2G3	9.8	0.2060	2.53	1.40	$6.08^{+0.43}_{-0.33}$	$0.32^{+0.08}_{-0.08}$	$0.0111^{+0.000257}_{-0.000256}$	1.1377	423	1.1374
A990	84070000	G2G3	14.0	0.1420	2.75	1.08	$6.40^{+0.30}_{-0.29}$	$0.17^{+0.05}_{-0.05}$	$0.0143^{+0.000205}_{-0.000204}$	0.9239	766	0.9237
A1060	80004000	G2G3	19.4	0.0124	0.41	5.01	$3.19^{+0.03}_{-0.03}$	$0.37^{+0.03}_{-0.02}$	$0.0952^{+0.000991}_{-0.000981}$	0.9916	924	0.9915
A1068	84064000	G2G3	14.7	0.1386	2.83	0.99	$4.11^{+0.15}_{-0.15}$	$0.36^{+0.07}_{-0.07}$	$0.0162^{+0.000351}_{-0.000346}$	0.9747	562	0.9745
A1204	82002000	G2G3	8.6	0.1706	1.94	1.40	$3.83^{+0.19}_{-0.18}$	$0.19^{+0.08}_{-0.08}$	$0.0106^{+0.000300}_{-0.000296}$	0.9983	328	0.9978
A1246	83007000	G2G3	9.8	0.2160	2.62	1.36	$5.30^{+0.30}_{-0.29}$	$0.26^{+0.08}_{-0.08}$	$0.00870^{+0.000214}_{-0.000211}$	1.0006	430	1.0003
A1367	81029000	G2G3	19.4	0.0214	0.70	2.16	$3.87^{+0.11}_{-0.11}$	$0.32^{+0.06}_{-0.06}$	$0.0588^{+0.00115}_{-0.00114}$	0.9210	506	0.9208
	81029010	G2G3	19.4		0.70		$3.82^{+0.13}_{-0.12}$	$0.17^{+0.05}_{-0.05}$	$0.0633^{+0.00131}_{-0.00129}$	1.1238	461	1.1235
	81030000	G2G3	19.4		0.70		$3.40^{+0.10}_{-0.09}$	$0.20^{+0.06}_{-0.06}$	$0.0647^{+0.00162}_{-0.00159}$	0.9889	441	0.9886
	81030010	G2G3	19.4		0.70		$3.55^{+0.08}_{-0.08}$	$0.26^{+0.05}_{-0.05}$	$0.0612^{+0.00128}_{-0.00125}$	1.0682	515	1.0679
	Combined						3.64 ± 0.10	0.23 ± 0.06	0.0618 ± 0.00133			
A1413	81008000	G2G3	19.4	0.1427	3.82	1.98	$7.32^{+0.26}_{-0.24}$	$0.29^{+0.05}_{-0.05}$	$0.0249^{+0.000296}_{-0.000295}$	1.1129	796	1.1128
A1553	84069000	G2G3	19.4	0.1652	4.27	1.99	$4.18^{+0.15}_{-0.15}$	$0.19^{+0.06}_{-0.06}$	$0.0255^{+0.000507}_{-0.000499}$	0.9996	639	0.9994
A1576	83014000	G2G3	7.4	0.3020	2.45	1.71	$6.57^{+0.56}_{-0.54}$	$0.42^{+0.12}_{-0.11}$	$0.00537^{+0.000166}_{-0.000164}$	0.9003	276	0.8997
A1650	84021000	G2G3	17.4	0.0840	2.21	1.53	$6.11^{+0.15}_{-0.14}$	$0.33^{+0.03}_{-0.03}$	$0.0373^{+0.000300}_{-0.000300}$	0.9980	993	0.9979
A1651	82036000	G2G3	16.9	0.0825	2.12	1.69	$6.21^{+0.18}_{-0.17}$	$0.29^{+0.04}_{-0.04}$	$0.0412^{+0.000390}_{-0.000390}$	1.1304	851	1.1303
A1656	80016000	G2G3	19.4	0.0231	0.75	0.90	$8.67^{+0.17}_{-0.17}$	$0.30^{+0.03}_{-0.03}$	$0.312^{+0.00191}_{-0.00195}$	1.0059	1002	1.0058
A1682	84075000	G2G3	13.3	0.2260	3.67	1.35	$7.24^{+0.68}_{-0.59}$	$0.21^{+0.11}_{-0.11}$	$0.00800^{+0.000220}_{-0.000218}$	1.0877	480	1.0874
A1689	80005000	G2G3	17.7	0.1784	4.13	1.87	$9.23^{+0.28}_{-0.28}$	$0.29^{+0.04}_{-0.04}$	$0.0305^{+0.000296}_{-0.000295}$	1.0308	871	1.0307
A1704	81007000	G2G3	8.3	0.0220	0.31	1.81	$4.08^{+0.31}_{-0.31}$	$0.00^{+0.11}_{-0.00}$	$0.00541^{+0.000141}_{-0.000220}$	1.0054	178	1.0042
A1736	83061000	G2G3	18.2	0.0431	1.27	4.99	$3.61^{+0.10}_{-0.10}$	$0.30^{+0.07}_{-0.07}$	$0.0307^{+0.000763}_{-0.000745}$	1.0719	501	1.0716
A1763	83044000	G2G3	9.1	0.1870	2.20	0.93	$7.30^{+0.46}_{-0.38}$	$0.12^{+0.07}_{-0.07}$	$0.0112^{+0.000197}_{-0.000196}$	0.9971	509	0.9969
A1772	81013000	G2G3	9.3	0.3058	3.10	4.29	$5.31^{+0.44}_{-0.42}$	$0.52^{+0.14}_{-0.13}$	$0.00388^{+0.000151}_{-0.000147}$	0.9157	287	0.9151
A1774	83049000	G2G3	9.1	0.1691	2.04	8.02	$5.59^{+0.28}_{-0.28}$	$0.08^{+0.06}_{-0.06}$	$0.0110^{+0.000222}_{-0.000231}$	1.0286	422	1.0283
A1775	85056000	G2G3	16.2	0.0696	1.75	1.07	$3.69^{+0.20}_{-0.11}$	$0.33^{+0.07}_{-0.08}$	$0.0197^{+0.000471}_{-0.000486}$	1.0129	606	1.0127
A1795	80006000	G2G3	18.9	0.0621	1.84	1.16	$5.80^{+0.07}_{-0.07}$	$0.36^{+0.02}_{-0.02}$	$0.0904^{+0.000534}_{-0.000531}$	1.0558	1083	1.0557
A1835	82052000	G2G3	14.5	0.2523	4.30	2.33	$7.88^{+0.49}_{-0.46}$	$0.22^{+0.07}_{-0.07}$	$0.0246^{+0.000430}_{-0.000431}$	0.9046	459	0.9044
	82052010	G2G3	15.5		4.59		$8.50^{+0.53}_{-0.52}$	$0.36^{+0.08}_{-0.08}$	$0.0246^{+0.000476}_{-0.000475}$	0.9727	442	0.9724
	Combined						8.17 ± 0.50	0.29 ± 0.07	0.0246 ± 0.000453			

Table A1. Broad-Band Single-Phase Plasma Fit Results – contd.

Object	Seq. Num.	Inst.	$A_{\rm out}$ (′)	z	$R_{\rm out}$ (Mpc)	$N_{\rm H}/10^{20}$ (cm^{-2})	$T_{\rm X}$ (keV)	Z (⊙)	$Norm.$ ($\frac{10^{-14}}{4\pi D_{\rm L}^2}\int n_e n_{\rm H} dV$)	χ^2_ν	$N_{\rm PI}$	$\chi^2_{\nu,{\rm reqd.}}$ for CF mod.
A1851	82007000	G2G3	6.9	0.2143	1.83	1.75	$4.26^{+0.52}_{-0.46}$	$0.08^{+0.18}_{-0.08}$	$0.00326^{+0.000209}_{-0.000198}$	0.9885	319	0.9880
A1895	83033000	G2G3	8.1	0.2250	2.23	1.97	$5.17^{+0.57}_{-0.52}$	$0.13^{+0.14}_{-0.13}$	$0.00493^{+0.000212}_{-0.000211}$	0.8868	175	0.8857
A1914	84032000	G2G3	15.2	0.1712	3.44	0.95	$10.53^{+0.51}_{-0.50}$	$0.25^{+0.06}_{-0.06}$	$0.0280^{+0.000342}_{-0.000342}$	0.9259	742	0.9258
A1942	83000000	G2G3	16.9	0.2240	4.63	2.58	$5.73^{+0.73}_{-0.60}$	$0.28^{+0.17}_{-0.15}$	$0.00722^{+0.000316}_{-0.000306}$	0.9548	459	0.9546
A1995	82005000	G2G3	8.3	0.3180	2.83	1.42	$7.57^{+1.07}_{-0.76}$	$0.21^{+0.15}_{-0.15}$	$0.00490^{+0.000185}_{-0.000182}$	1.0449	208	1.0439
A2029	81023000	G2	19.4	0.0765	2.27	3.07	$8.22^{+0.21}_{-0.21}$	$0.32^{+0.03}_{-0.03}$	$0.107^{+0.000769}_{-0.000827}$	1.0475	547	1.0473
A2034	84022000	G2G3	16.5	0.1510	3.40	1.58	$7.93^{+0.34}_{-0.34}$	$0.17^{+0.04}_{-0.04}$	$0.0238^{+0.000274}_{-0.000277}$	1.0919	783	1.0917
A2052	85061000	G2G3	17.7	0.0348	1.01	2.91	$3.03^{+0.04}_{-0.04}$	$0.39^{+0.03}_{-0.03}$	$0.0605^{+0.000806}_{-0.000798}$	1.0142	862	1.0141
A2063	81002000	G2	17.4	0.0355	1.01	2.91	$3.52^{+0.09}_{-0.09}$	$0.27^{+0.06}_{-0.06}$	$0.0545^{+0.00120}_{-0.00118}$	0.9938	342	0.9934
A2065	84054000	G2G3	19.4	0.0722	2.16	2.87	$5.36^{+0.13}_{-0.13}$	$0.27^{+0.04}_{-0.04}$	$0.0420^{+0.000488}_{-0.000482}$	1.1037	769	1.1035
	84054010	G2G3	17.2		1.92		$5.47^{+0.14}_{-0.14}$	$0.29^{+0.04}_{-0.04}$	$0.0407^{+0.000487}_{-0.000481}$	0.9796	709	0.9795
	Combined						5.42 ± 0.13	0.28 ± 0.04	0.0414 ± 0.000484			
A2104	84072000	G2G3	17.2	0.1554	3.62	8.69	$9.12^{+0.48}_{-0.46}$	$0.18^{+0.07}_{-0.07}$	$0.0166^{+0.000240}_{-0.000241}$	1.0281	777	1.0279
A2107	85060000	G2G3	17.4	0.0421	1.19	4.50	$3.93^{+0.10}_{-0.10}$	$0.32^{+0.05}_{-0.05}$	$0.0283^{+0.000482}_{-0.000479}$	0.9241	680	0.9239
A2142	81004000	G2	19.4	0.0899	2.62	3.88	$9.02^{+0.32}_{-0.31}$	$0.31^{+0.05}_{-0.05}$	$0.1000^{+0.00110}_{-0.00110}$	0.9087	457	0.9085
A2147	83074000	G2G3	19.4	0.0356	1.13	3.28	$4.50^{+0.07}_{-0.07}$	$0.23^{+0.03}_{-0.03}$	$0.0598^{+0.000547}_{-0.000542}$	1.0646	936	1.0645
A2151	83030000	G2G3	18.2	0.0370	1.10	3.38	$2.40^{+0.06}_{-0.06}$	$0.50^{+0.10}_{-0.09}$	$0.0228^{+0.00110}_{-0.00107}$	1.0108	542	1.0105
A2163	80024000	G2G3	16.0	0.2030	4.10	11.00	$13.29^{+0.64}_{-0.64}$	$0.18^{+0.06}_{-0.06}$	$0.0464^{+0.000510}_{-0.000507}$	0.9207	838	0.9206
A2199	80023000	G2G3	19.4	0.0299	0.96	0.87	$4.27^{+0.04}_{-0.04}$	$0.36^{+0.02}_{-0.02}$	$0.131^{+0.000822}_{-0.000763}$	1.0688	1077	1.0687
A2204	82045000	G2G3	18.7	0.1523	3.87	5.61	$6.99^{+0.24}_{-0.23}$	$0.38^{+0.05}_{-0.05}$	$0.0504^{+0.000628}_{-0.000625}$	1.0412	657	1.0410
	82045010		17.7		3.67		$7.47^{+0.31}_{-0.23}$	$0.40^{+0.05}_{-0.05}$	$0.0485^{+0.000562}_{-0.000561}$	1.0436	699	1.0435
	Combined						7.21 ± 0.25	0.39 ± 0.05	0.0494 ± 0.000594			
A2218	80001000	G2G3	14.7	0.1710	3.32	3.34	$6.84^{+0.34}_{-0.34}$	$0.17^{+0.06}_{-0.06}$	$0.0137^{+0.000232}_{-0.000231}$	0.9988	585	0.9986
A2219	82037000	G2G3	14.0	0.2281	3.88	1.75	$9.52^{+0.55}_{-0.40}$	$0.24^{+0.06}_{-0.06}$	$0.0243^{+0.000327}_{-0.000324}$	0.9254	680	0.9253
A2255	84012000	G2G3	17.9	0.0808	2.20	2.60	$6.68^{+0.18}_{-0.18}$	$0.25^{+0.04}_{-0.04}$	$0.0299^{+0.000297}_{-0.000296}$	0.9649	912	0.9648
	84012010	G2G3	16.9		2.08		$7.11^{+0.22}_{-0.22}$	$0.14^{+0.04}_{-0.04}$	$0.0288^{+0.000306}_{-0.000305}$	0.9751	820	0.9750
	Combined						6.87 ± 0.20	0.20 ± 0.04	0.0294 ± 0.000301			
A2256	10004030	G2G3	18.9	0.0581	1.73	4.30	$6.94^{+0.12}_{-0.12}$	$0.24^{+0.02}_{-0.02}$	$0.0861^{+0.000564}_{-0.000564}$	1.0546	1005	1.0545
	80002000	G2G3	18.9		1.73		$6.98^{+0.11}_{-0.11}$	$0.27^{+0.02}_{-0.02}$	$0.0845^{+0.000472}_{-0.000471}$	1.0562	1090	1.0561
	Combined						6.96 ± 0.11	0.25 ± 0.02	0.0852 ± 0.000518			
A2261	84062000	G2G3	16.2	0.2240	4.44	3.28	$7.49^{+0.57}_{-0.43}$	$0.27^{+0.08}_{-0.08}$	$0.0189^{+0.000400}_{-0.000393}$	1.1054	477	1.1051
A2319	80041000	G2G3	19.4	0.0564	1.73	8.59	$9.54^{+0.32}_{-0.18}$	$0.25^{+0.03}_{-0.03}$	$0.165^{+0.00102}_{-0.00111}$	0.9702	1010	0.9701
	80041010	G2G3	19.4		1.73		$9.96^{+0.30}_{-0.28}$	$0.25^{+0.03}_{-0.03}$	$0.157^{+0.00113}_{-0.00104}$	0.9533	976	0.9532
	Combined						9.73 ± 0.27	0.25 ± 0.03	0.161 ± 0.00107			
A2390	82032000	G2G3	13.3	0.1237	2.34	7.00	$11.25^{+0.88}_{-0.95}$	$0.00^{+0.07}_{-0.00}$	$0.0225^{+0.000343}_{-0.000363}$	0.9674	299	0.9668
	82032010	G2G3	14.2		2.50		$10.07^{+1.03}_{-1.00}$	$0.00^{+0.11}_{-0.00}$	$0.0211^{+0.000371}_{-0.000486}$	0.9875	241	0.9868
	82032020	G2G3	11.8		2.07		$10.47^{+1.37}_{-1.25}$	$0.13^{+0.14}_{-0.13}$	$0.0210^{+0.000658}_{-0.000660}$	0.8515	164	0.8503
	Combined						10.63 ± 1.08	0.02 ± 0.07	0.0217 ± 0.000480			
A2440	81033000	G2G3	19.4	0.0904	2.63	5.16	$3.88^{+0.14}_{-0.14}$	$0.18^{+0.06}_{-0.06}$	$0.0191^{+0.000413}_{-0.000408}$	1.0100	685	1.0098
A2597	83062000	G2G3	16.5	0.0852	2.12	2.48	$3.63^{+0.06}_{-0.06}$	$0.33^{+0.04}_{-0.04}$	$0.0340^{+0.000452}_{-0.000446}$	1.1048	786	1.1047
A2634	83002000	G2G3	19.4	0.0309	0.99	4.88	$3.27^{+0.07}_{-0.07}$	$0.28^{+0.05}_{-0.05}$	$0.0296^{+0.000623}_{-0.000614}$	1.0108	769	1.0107
A2657	84002000	G2G3	18.2	0.0414	1.22	6.00	$3.81^{+0.07}_{-0.07}$	$0.22^{+0.03}_{-0.03}$	$0.0382^{+0.000458}_{-0.000454}$	1.0627	870	1.0626
A2670	82049000	G2G3	17.2	0.0759	2.00	2.69	$3.73^{+0.17}_{-0.13}$	$0.12^{+0.07}_{-0.07}$	$0.0179^{+0.000471}_{-0.000468}$	1.0169	524	1.0167
A2811	84003000	G2G3	14.2	0.1090	2.25	1.54	$5.31^{+0.17}_{-0.16}$	$0.18^{+0.04}_{-0.04}$	$0.0183^{+0.000241}_{-0.000239}$	1.0727	733	1.0726
A3112	81003000	G2G3	17.4	0.0746	2.00	4.00	$4.45^{+0.07}_{-0.07}$	$0.45^{+0.04}_{-0.04}$	$0.0454^{+0.000478}_{-0.000473}$	1.0022	870	1.0021
A3158	84020000	G2G3	18.9	0.0575	1.72	1.20	$5.77^{+0.10}_{-0.05}$	$0.26^{+0.03}_{-0.03}$	$0.0515^{+0.000441}_{-0.000438}$	1.0445	921	1.0444
A3221	83048000	G2G3	17.7	0.1044	2.71	2.66	$5.48^{+0.20}_{-0.19}$	$0.30^{+0.06}_{-0.05}$	$0.0259^{+0.000413}_{-0.000409}$	0.9881	629	0.9879
A3266	83023000	G2G3	19.4	0.0545	1.68	3.00	$8.34^{+0.17}_{-0.16}$	$0.26^{+0.03}_{-0.03}$	$0.0828^{+0.000496}_{-0.000498}$	1.0280	1068	1.0280
A3376	84056000	G2G3	18.9	0.0490	1.49	4.41	$4.38^{+0.13}_{-0.13}$	$0.22^{+0.05}_{-0.05}$	$0.0319^{+0.000570}_{-0.000560}$	0.8889	621	0.8887
A3391	72019000	G2G3	19.2	0.0540	1.65	4.50	$5.60^{+0.17}_{-0.17}$	$0.34^{+0.05}_{-0.05}$	$0.0351^{+0.000518}_{-0.000511}$	1.0459	669	1.0458
A3526	80032000	G2G3	19.4	0.0107	0.36	7.96	$3.38^{+0.03}_{-0.03}$	$0.66^{+0.03}_{-0.03}$	$0.184^{+0.00173}_{-0.00173}$	1.1637	973	1.1636
	83026000	G2G3	19.4		0.36		$3.45^{+0.01}_{-0.01}$	$0.60^{+0.01}_{-0.01}$	$0.186^{+0.000867}_{-0.000904}$	1.5362	1209	1.5361
	Combined						3.42 ± 0.02	0.62 ± 0.02	0.185 ± 0.00131			
A3558	82046000	G2G3	19.4	0.0476	1.48	4.00	$5.49^{+0.10}_{-0.10}$	$0.30^{+0.03}_{-0.03}$	$0.0952^{+0.000837}_{-0.000834}$	1.0808	847	1.0806
	83058000	G2G3	19.4		1.48		$5.56^{+0.09}_{-0.09}$	$0.35^{+0.03}_{-0.03}$	$0.0796^{+0.000598}_{-0.000594}$	1.1955	944	1.1953
	Combined						5.53 ± 0.09	0.32 ± 0.03	0.0861 ± 0.000716			
A3562	84041000	G2G3	19.4	0.0478	1.49	4.20	$5.16^{+0.16}_{-0.16}$	$0.34^{+0.05}_{-0.05}$	$0.0401^{+0.000593}_{-0.000588}$	0.9655	661	0.9654
A3571	82047000	G2G3	19.4	0.0390	1.23	4.04	$7.24^{+0.09}_{-0.09}$	$0.37^{+0.02}_{-0.02}$	$0.156^{+0.000759}_{-0.000770}$	1.0508	1125	1.0508
A3627	84005000	G2G3	19.4	0.0164	0.54	20.20	$6.02^{+0.08}_{-0.08}$	$0.26^{+0.02}_{-0.02}$	$0.154^{+0.000648}_{-0.000724}$	1.2336	1148	1.2335

Table A1. Broad-Band Single-Phase Plasma Fit Results – contd.

Object	Seq. Num.	Inst.	$A_{\rm out}$ (′)	z	$R_{\rm out}$ (Mpc)	$N_{\rm H}/10^{20}$ (cm^{-2})	$T_{\rm X}$ (keV)	Z (⊙)	$Norm.$ $(\frac{10^{-14}}{4\pi D_{\rm L}^2}\int n_{\rm e}n_{\rm H}dV)$	χ^2_ν	$N_{\rm PI}$	$\chi^2_{\nu,{\rm reqd.}}$ for CF mod.
A3667	83054000	G2G3	19.4	0.0585	1.79	4.00	$7.13^{+0.14}_{-0.14}$	$0.25^{+0.03}_{-0.03}$	$0.0943^{+0.000730}_{-0.000728}$	0.9051	903	0.9050
A3921	83048010	G2G3	18.2	0.0784	2.18	2.94	$5.73^{+0.24}_{-0.23}$	$0.20^{+0.06}_{-0.06}$	$0.0251^{+0.000435}_{-0.000429}$	0.9901	548	0.9899
A4059	82030000	G2G3	19.4	0.0478	1.49	1.10	$3.90^{+0.07}_{-0.07}$	$0.50^{+0.04}_{-0.04}$	$0.0441^{+0.000545}_{-0.000543}$	0.9779	866	0.9778
2A0336	82029000	G2G3	19.4	0.0350	1.12	17.20	$3.08^{+0.03}_{-0.03}$	$0.39^{+0.03}_{-0.03}$	$0.124^{+0.00130}_{-0.00131}$	1.0012	885	1.0011
	82040000	G2	17.9		1.03		$3.08^{+0.04}_{-0.03}$	$0.37^{+0.03}_{-0.03}$	$0.118^{+0.00141}_{-0.00148}$	1.0313	500	1.0310
	Combined						3.08 ± 0.03	0.38 ± 0.03	0.121 ± 0.00138			
AWM4	83072000	G2G3	17.2	0.0424	1.18	4.93	$2.38^{+0.06}_{-0.06}$	$0.30^{+0.03}_{-0.07}$	$0.0175^{+0.000767}_{-0.000746}$	1.1173	667	1.1171
AWM7	80036000	G2G3	19.4	0.0176	0.58	9.19	$3.79^{+0.05}_{-0.05}$	$0.48^{+0.03}_{-0.03}$	$0.158^{+0.00157}_{-0.00150}$	1.0069	883	1.0068
CL0016	80025000	G2G3	9.6	0.5500	4.25	3.21	$7.54^{+0.13}_{-0.66}$	$0.12^{+0.13}_{-0.12}$	$0.00599^{+0.000226}_{-0.000235}$	1.0616	236	1.0608
	84016000	G2G3	9.1		4.03		$8.82^{+0.88}_{-0.81}$	$0.35^{+0.13}_{-0.12}$	$0.00544^{+0.000186}_{-0.000186}$	0.8543	381	0.8540
	Combined						8.15 ± 0.80	0.24 ± 0.12	0.00569 ± 0.000208			
Cygnus-A	70003000	G2G3	19.4	0.0575	1.76	36.10	$9.34^{+0.17}_{-0.17}$	$0.66^{+0.03}_{-0.03}$	$0.108^{+0.000759}_{-0.000667}$	1.3730	1111	1.3729
	70003010	G2G3	19.4		1.76		$9.74^{+0.21}_{-0.37}$	$0.68^{+0.03}_{-0.03}$	$0.105^{+0.000562}_{-0.000590}$	1.6954	1177	1.6953
	Combined						9.49 ± 0.23	0.67 ± 0.03	0.107 ± 0.000645			
Klemola44	83004000	G2G3	18.4	0.0283	0.86	1.56	$3.15^{+0.03}_{-0.03}$	$0.35^{+0.03}_{-0.03}$	$0.0641^{+0.000726}_{-0.000718}$	1.0213	936	1.0212
MKW3s	80011000	G2G3	18.7	0.0434	1.31	2.89	$3.41^{+0.05}_{-0.05}$	$0.37^{+0.04}_{-0.04}$	$0.0513^{+0.000744}_{-0.000737}$	0.9578	776	0.9577
MKW4s	83008000	G2G3	16.2	0.0288	0.77	1.66	$1.93^{+0.09}_{-0.08}$	$0.16^{+0.11}_{-0.09}$	$0.00966^{+0.000857}_{-0.000821}$	0.9995	508	0.9992
MKW9	83009000	G2G3	12.5	0.0397	0.81	4.11	$1.83^{+0.10}_{-0.08}$	$0.25^{+0.15}_{-0.12}$	$0.00665^{+0.000812}_{-0.000730}$	1.0170	407	1.0167
Ophiuchus	80027000	G2G3	19.4	0.0280	0.90	19.70	$12.75^{+0.29}_{-0.29}$	$0.34^{+0.03}_{-0.03}$	$0.516^{+0.00271}_{-0.00260}$	1.0864	1166	1.0864
PKS0745-19	81016000	G2G3	17.4	0.1028	2.63	35.00	$7.21^{+0.11}_{-0.11}$	$0.31^{+0.03}_{-0.02}$	$0.0929^{+0.000527}_{-0.000527}$	1.0124	1080	1.0123
SC1327	83059000	G2G3	19.4	0.0476	1.48	4.00	$3.62^{+0.08}_{-0.08}$	$0.15^{+0.04}_{-0.04}$	$0.0372^{+0.000671}_{-0.000657}$	1.0394	724	1.0392
Tri.Aus.	83060000	G2G3	19.4	0.0510	1.58	12.70	$10.31^{+0.27}_{-0.27}$	$0.26^{+0.03}_{-0.03}$	$0.172^{+0.00115}_{-0.00113}$	0.9858	1004	0.9857
	83060010	G2G3	19.4		1.58		$10.30^{+0.41}_{-0.43}$	$0.28^{+0.05}_{-0.05}$	$0.159^{+0.00156}_{-0.00163}$	0.9621	756	0.9620
	Combined						10.31 ± 0.34	0.26 ± 0.04	0.166 ± 0.00136			
Virgo	60033000	G2G3	19.4	0.0036	0.12	2.50	$2.40^{+0.01}_{-0.01}$	$0.43^{+0.02}_{-0.01}$	$0.515^{+0.00412}_{-0.00416}$	1.3231	997	1.3230
Zw3146	80014000	G2G3	9.1	0.2906	2.95	3.01	$5.89^{+0.30}_{-0.22}$	$0.35^{+0.06}_{-0.06}$	$0.0172^{+0.000312}_{-0.000309}$	1.0282	523	1.0280

Table A2. Broad-Band Cooling Flow Spectral Fit Results

Object	Seq. Num.	Inst.	$A_{\rm out}$ (′)	z	$R_{\rm out}$ (Mpc)	$N_{\rm H}/10^{20}$ (cm^{-2})	$T_{\rm X}$ (keV)	Z (⊙)	Norm. ($\frac{10^{-14}}{4\pi D_{\rm L}^2}\int n_e n_{\rm H} dV$)	$\dot{M}$ (M$_\odot$ yr^{-1})	χ^2_ν	$N_{\rm PI}$
A85	81024000	G2G3	19.4	0.0521	1.61	3.01	$6.47^{+0.33}_{-0.29}$	$0.39^{+0.02}_{-0.02}$	$0.0910^{+0.00514}_{-0.00557}$	147^{+72}_{-72}	1.0737	1068
	81024010	G2G3	19.4		1.61		$7.35^{+0.82}_{-0.57}$	$0.38^{+0.04}_{-0.04}$	$0.0732^{+0.00923}_{-0.0102}$	341^{+93}_{-104}	0.9598	836
	Combined						6.74 ± 0.50	0.38 ± 0.03	0.0846 ± 0.00753	229 ± 85		
A119	83045000	G2G3	19.4	0.0443	1.39	3.45	$6.05^{+0.55}_{-0.43}$	$0.27^{+0.03}_{-0.04}$	$0.0436^{+0.00473}_{-0.00445}$	52^{+42}_{-51}	1.1024	907
A262	81031000	G2G3	19.4	0.0163	0.54	5.33	$2.29^{+0.12}_{-0.09}$	$0.30^{+0.05}_{-0.05}$	$0.0641^{+0.00697}_{-0.00692}$	26^{+27}_{-26}	1.1456	646
A370	80010000	G2G3	7.9	0.3730	2.94	3.02	$5.71^{+0.77}_{-0.53}$	$0.53^{+0.17}_{-0.16}$	$0.00401^{+0.000182}_{-0.000652}$	0^{+424}_{0}	0.9070	242
A399	82008000	G2G3	19.4	0.0715	2.14	17.10	$9.55^{+1.92}_{-0.96}$	$0.32^{+0.04}_{-0.04}$	$0.0319^{+0.00548}_{-0.00780}$	368^{+81}_{-82}	0.9691	911
A400	83037000	G2G3	19.4	0.0238	0.77	8.82	$2.36^{+0.14}_{-0.11}$	$0.29^{+0.07}_{-0.06}$	$0.0255^{+0.00301}_{-0.00315}$	24^{+24}_{-24}	1.0873	754
A401	82010000	G2G3	19.4	0.0748	2.23	11.10	$10.68^{+1.11}_{-0.94}$	$0.29^{+0.03}_{-0.03}$	$0.0665^{+0.00621}_{-0.00712}$	326^{+106}_{-108}	1.0462	1091
A426	80007000	G2G3	19.4	0.0179	0.59	14.51	$7.71^{+0.29}_{-0.37}$	$0.44^{+0.01}_{-0.01}$	$0.537^{+0.0463}_{-0.0327}$	671^{+28}_{-45}	1.1640	1272
A478	81015000	G2	18.4	0.0881	2.44	27.50	$7.42^{+0.71}_{-0.54}$	$0.32^{+0.03}_{-0.03}$	$0.0877^{+0.0102}_{-0.00996}$	636^{+286}_{-345}	0.9366	534
A496	80003000	G2G3	19.4	0.0330	1.05	4.41	$4.51^{+0.17}_{-0.15}$	$0.38^{+0.02}_{-0.02}$	$0.0880^{+0.00545}_{-0.00598}$	138^{+42}_{-41}	1.0225	1063
A521	84071000	G2G3	13.3	0.2533	3.95	5.81	$5.89^{+1.06}_{-0.32}$	$0.29^{+0.09}_{-0.08}$	$0.00989^{+0.000639}_{-0.00209}$	0^{+587}_{0}	0.9424	506
A539	83003000	G2G3	17.9	0.0288	0.86	13.30	$3.67^{+0.36}_{-0.34}$	$0.21^{+0.05}_{-0.04}$	$0.0231^{+0.00639}_{-0.00745}$	120^{+28}_{-38}	1.0098	707
A548	84034000	G2G3	18.2	0.0415	1.23	2.04	$3.10^{+0.12}_{-0.10}$	$0.35^{+0.08}_{-0.09}$	$0.0191^{+0.000367}_{-0.000920}$	0^{+17}_{0}	0.9568	547
A576	84001000	G2G3	17.9	0.0381	1.11	5.65	$4.02^{+0.20}_{-0.07}$	$0.34^{+0.04}_{-0.04}$	$0.0359^{+0.000404}_{-0.00250}$	0^{+29}_{0}	1.0818	885
A586	81009010	G2	11.3	0.1710	2.55	5.72	$6.82^{+12.18}_{-1.26}$	$0.21^{+0.13}_{-0.13}$	$0.0111^{+0.00249}_{-0.0111}$	271^{+596}_{-271}	1.1231	156
A611	84063000	G2G3	8.6	0.2880	2.77	4.99	$6.86^{+0.48}_{-0.45}$	$0.21^{+0.08}_{-0.08}$	$0.00549^{+0.000128}_{-0.000358}$	0^{+117}_{0}	0.8726	428
A644	83022000	G2G3	17.7	0.0704	1.93	7.32	$7.47^{+0.32}_{-0.10}$	$0.33^{+0.02}_{-0.02}$	$0.0639^{+0.000323}_{-0.00268}$	0^{+60}_{0}	1.0643	1124
A665	80035000	G2G3	12.8	0.1816	3.02	4.21	$7.90^{+1.45}_{-0.52}$	$0.29^{+0.06}_{-0.06}$	$0.0174^{+0.000790}_{-0.00322}$	56^{+374}_{-56}	1.0907	623
A697	84031000	G2G3	13.0	0.2820	4.13	3.24	$8.59^{+0.52}_{-0.46}$	$0.29^{+0.07}_{-0.07}$	$0.0126^{+0.000194}_{-0.000584}$	0^{+156}_{0}	1.0815	664
A754	82057000	G2G3	19.4	0.0542	1.67	4.74	$12.85^{+1.77}_{-1.35}$	$0.30^{+0.04}_{-0.04}$	$0.0822^{+0.00884}_{-0.00987}$	218^{+63}_{-70}	1.0901	1038
A773	82001000	G2G3	13.8	0.1970	3.46	1.44	$8.63^{+2.30}_{-0.64}$	$0.10^{+0.09}_{-0.09}$	$0.0107^{+0.000213}_{-0.00226}$	0^{+292}_{0}	1.0192	529
A780	80015000	G2G3	17.2	0.0522	1.43	4.80	$4.49^{+0.41}_{-0.37}$	$0.29^{+0.04}_{-0.04}$	$0.0415^{+0.00839}_{-0.00776}$	492^{+99}_{-134}	1.1051	690
A854	83006000	G2G3	11.1	0.2069	2.88	3.12	$6.05^{+0.77}_{-0.36}$	$0.09^{+0.10}_{-0.09}$	$0.00588^{+9.00}_{-0.000670}$	0^{+129}_{0}	0.9836	418
A963	80000000	G2G3	9.8	0.2060	2.53	1.40	$6.08^{+0.81}_{-0.31}$	$0.32^{+0.08}_{-0.08}$	$0.0111^{+0.000211}_{-0.00163}$	0^{+319}_{0}	1.1405	423
A990	84070000	G2G3	14.0	0.1420	2.75	1.08	$8.47^{+2.48}_{-1.77}$	$0.16^{+0.06}_{-0.07}$	$0.00981^{+0.00359}_{-0.00359}$	348^{+176}_{-260}	0.9228	766
A1060	80004000	G2G3	19.4	0.0124	0.41	5.01	$3.27^{+0.11}_{-0.09}$	$0.36^{+0.03}_{-0.03}$	$0.0913^{+0.00445}_{-0.00520}$	6^{+8}_{-6}	0.9919	924
A1068	84064000	G2G3	14.7	0.1386	2.83	0.99	$4.11^{+0.18}_{-0.14}$	$0.37^{+0.07}_{-0.07}$	$0.0162^{+0.000334}_{-0.000838}$	0^{+119}_{0}	0.9765	562
A1204	82002000	G2G3	8.6	0.1706	1.94	1.40	$4.70^{+1.97}_{-0.80}$	$0.16^{+0.08}_{-0.08}$	$0.00684^{+0.00328}_{-0.00458}$	675^{+376}_{-560}	0.9970	328
A1246	83007000	G2G3	9.8	0.2160	2.62	1.36	$5.31^{+0.65}_{-0.28}$	$0.26^{+0.08}_{-0.07}$	$0.00870^{+0.000203}_{-0.00147}$	0^{+343}_{0}	1.0030	430
A1367	81029000	G2G3	19.4	0.0214	0.70	2.16	$4.70^{+0.74}_{-0.50}$	$0.27^{+0.06}_{-0.05}$	$0.0413^{+0.00965}_{-0.0106}$	57^{+21}_{-28}	0.9149	506
	81029010	G2G3	19.4		0.70		$4.23^{+0.76}_{-0.43}$	$0.15^{+0.06}_{-0.06}$	$0.0529^{+0.0105}_{-0.0145}$	35^{+37}_{-35}	1.1241	461
	81030000	G2G3	19.4		0.70		$3.51^{+0.39}_{-0.20}$	$0.18^{+0.07}_{-0.06}$	$0.0607^{+0.00561}_{-0.0114}$	17^{+40}_{-17}	0.9909	441
	81030010	G2G3	19.4		0.70		$4.01^{+0.45}_{-0.37}$	$0.22^{+0.06}_{-0.06}$	$0.0493^{+0.00896}_{-0.0114}$	44^{+31}_{-32}	1.0670	515
	Combined						3.99 ± 0.48	0.20 ± 0.06	0.0514 ± 0.0103	39 ± 30		
A1413	81008000	G2G3	19.4	0.1427	3.82	1.98	$8.00^{+1.28}_{-0.86}$	$0.29^{+0.05}_{-0.05}$	$0.0225^{+0.00269}_{-0.00380}$	210^{+263}_{-210}	1.1137	796
A1553	84069000	G2G3	19.4	0.1652	4.27	1.99	$9.16^{+1.02}_{-0.64}$	$0.16^{+0.06}_{-0.06}$	$0.00105^{+0.00364}_{-0.00105}$	2237^{+124}_{-127}	0.9718	639
A1576	83014000	G2G3	7.4	0.3020	2.45	1.71	$6.57^{+0.95}_{-0.52}$	$0.42^{+0.12}_{-0.11}$	$0.00536^{+0.000156}_{-0.000920}$	0^{+346}_{0}	0.9036	276
A1650	84021000	G2G3	17.4	0.0840	2.21	1.53	$6.55^{+0.51}_{-0.43}$	$0.33^{+0.03}_{-0.03}$	$0.0341^{+0.00284}_{-0.00321}$	115^{+102}_{-102}	0.9977	993
A1651	82036000	G2G3	16.9	0.0825	2.12	1.69	$7.15^{+0.84}_{-0.62}$	$0.29^{+0.04}_{-0.04}$	$0.0341^{+0.00436}_{-0.00484}$	231^{+121}_{-132}	1.1282	851
A1656	80016000	G2G3	19.4	0.0231	0.75	0.90	$10.03^{+0.89}_{-0.81}$	$0.30^{+0.03}_{-0.03}$	$0.269^{+0.0218}_{-0.0205}$	87^{+34}_{-42}	1.0027	1002
A1682	84075000	G2G3	13.3	0.2260	3.67	1.35	$7.25^{+0.92}_{-0.55}$	$0.21^{+0.11}_{-0.11}$	$0.00800^{+0.000204}_{-0.000946}$	0^{+189}_{0}	1.0900	480
A1689	80005000	G2G3	17.7	0.1784	4.13	1.87	$9.48^{+1.36}_{-0.52}$	$0.30^{+0.05}_{-0.04}$	$0.0295^{+0.00134}_{-0.00374}$	118^{+375}_{-118}	1.0319	871
A1704	81007000	G2G3	8.3	0.0220	0.31	1.81	$6.45^{+4.27}_{-2.30}$	0.00 ± 0.05	$0.00194^{+0.00319}_{-0.00194}$	7^{+1}_{-6}	1.0041	178
A1736	83061000	G2G3	18.2	0.0431	1.27	4.99	$4.02^{+0.67}_{-0.43}$	$0.27^{+0.07}_{-0.07}$	$0.0255^{+0.00538}_{-0.00710}$	79^{+74}_{-79}	1.0721	501
A1763	83044000	G2G3	9.1	0.1870	2.20	0.93	$7.30^{+1.65}_{-0.37}$	$0.13^{+0.07}_{-0.07}$	$0.0112^{+0.000187}_{-0.00232}$	0^{+295}_{0}	0.9991	509
A1772	81013000	G2G3	9.3	0.3058	3.10	4.29	$5.32^{+1.06}_{-0.40}$	$0.52^{+0.14}_{-0.13}$	$0.00388^{+0.000441}_{-0.00106}$	0^{+482}_{0}	0.9189	287
A1774	83049000	G2G3	9.1	0.1691	2.04	8.02	$14.57^{+1.28}_{-2.46}$	$0.07^{+0.08}_{-0.07}$	0.00 ± 0.00301	732^{+58}_{-53}	0.9901	422
A1775	85056000	G2G3	16.2	0.0696	1.75	1.07	$8.70^{+0.42}_{-2.63}$	$0.27^{+0.07}_{-0.07}$	0.00 ± 0.00653	366^{+18}_{-17}	0.9851	606
A1795	80006000	G2G3	18.9	0.0621	1.84	1.16	$7.26^{+0.51}_{-0.40}$	$0.36^{+0.02}_{-0.02}$	$0.0658^{+0.00585}_{-0.00632}$	453^{+86}_{-90}	1.0357	1083
A1835	82052000	G2G3	14.5	0.2523	4.30	2.33	$12.09^{+14.55}_{-3.18}$	$0.25^{+0.09}_{-0.08}$	$0.0133^{+0.00730}_{-0.0133}$	1978^{+673}_{-1100}	0.9006	459
	82052010	G2G3	15.5		4.59		$8.50^{+1.50}_{-0.50}$	$0.36^{+0.08}_{-0.08}$	$0.0246^{+0.000448}_{-0.00440}$	0^{+937}_{0}	0.9750	442
	Combined						8.86 ± 4.93	0.31 ± 0.08	0.0225 ± 0.00636	683 ± 677		

Table A2. Broad-Band Cooling Flow Spectral Fit Results – contd.

Object	Seq. Num.	Inst.	A_{out} (′)	z	R_{out} (Mpc)	$N_{\mathrm{H}}/10^{20}$ (cm^{-2})	T_{X} (keV)	Z (⊙)	$Norm.$ ($\frac{10^{-14}}{4\pi D_{\mathrm{L}}^2}\int n_{\mathrm{e}}n_{\mathrm{H}}dV$)	$\dot{M}$ (M$_\odot$ yr^{-1})	χ^2_ν	N_{PI}
A1851	82007000	G2G3	6.9	0.2143	1.83	1.75	$4.23^{+0.60}_{-0.42}$	$0.08^{+0.18}_{-0.08}$	$0.00326^{+0.000187}_{-0.000599}$	0^{+150}_{0}	0.9916	319
A1895	83033000	G2G3	8.1	0.2250	2.23	1.97	$5.18^{+1.70}_{-0.52}$	$0.13^{+0.14}_{-0.13}$	$0.00492^{+0.000735}_{-0.00193}$	0^{+411}_{0}	0.8920	175
A1914	84032000	G2G3	15.2	0.1712	3.44	0.95	$11.70^{+3.57}_{-1.58}$	$0.26^{+0.07}_{-0.06}$	$0.0252^{+0.00312}_{-0.00586}$	256^{+390}_{-256}	0.9266	742
A1942	83000000	G2G3	16.9	0.2240	4.63	2.58	$15.60^{+3.44}_{-4.65}$	$0.30^{+0.20}_{-0.19}$	$(3.44^{+6.94}_{-3.44})\times10^{-08}$	817^{+118}_{-741}	0.9543	459
A1995	82005000	G2G3	8.3	0.3180	2.83	1.42	$7.58^{+2.99}_{-0.74}$	$0.21^{+0.15}_{-0.15}$	$0.00490^{+0.000177}_{-0.00171}$	0^{+517}_{0}	1.0500	208
A2029	81023000	G2	19.4	0.0765	2.27	3.07	$8.22^{+0.58}_{-0.20}$	$0.32^{+0.03}_{-0.03}$	$0.107^{+0.000721}_{-0.00736}$	0^{+175}_{0}	1.0494	547
A2034	84022000	G2G3	16.5	0.1510	3.40	1.58	$9.55^{+1.55}_{-1.38}$	$0.18^{+0.05}_{-0.05}$	$0.0187^{+0.00379}_{-0.00311}$	400^{+181}_{-312}	1.0912	783
A2052	85061000	G2G3	17.7	0.0348	1.01	2.91	$3.30^{+0.16}_{-0.13}$	$0.35^{+0.04}_{-0.04}$	$0.0514^{+0.00419}_{-0.00479}$	120^{+51}_{-51}	1.0087	862
A2063	81002000	G2	17.4	0.0355	1.01	2.91	$3.90^{+0.51}_{-0.38}$	$0.24^{+0.06}_{-0.06}$	$0.0450^{+0.00897}_{-0.00975}$	99^{+77}_{-93}	0.9934	342
A2065	84054000	G2G3	19.4	0.0722	2.16	2.87	$6.45^{+0.89}_{-0.68}$	$0.26^{+0.04}_{-0.04}$	$0.0318^{+0.00545}_{-0.00613}$	273^{+117}_{-132}	1.1005	769
	84054010	G2G3	17.2		1.92		$6.00^{+0.70}_{-0.52}$	$0.28^{+0.04}_{-0.04}$	$0.0353^{+0.00545}_{-0.00493}$	155^{+115}_{-147}	0.9794	709
	Combined						6.19 ± 0.70	0.27 ± 0.04	0.0337 ± 0.00543	216 ± 128		
A2104	84072000	G2G3	17.2	0.1554	3.62	8.69	$9.13^{+0.69}_{-0.45}$	$0.18^{+0.07}_{-0.06}$	$0.0166^{+0.000223}_{-0.00113}$	0^{+94}_{0}	1.0294	777
A2107	85060000	G2G3	17.4	0.0421	1.19	4.50	$4.31^{+0.57}_{-0.35}$	$0.30^{+0.05}_{-0.05}$	$0.0242^{+0.00360}_{-0.00496}$	57^{+52}_{-48}	0.9234	680
A2142	81004000	G2	19.4	0.0899	2.62	3.88	$10.96^{+2.56}_{-1.58}$	$0.33^{+0.06}_{-0.06}$	$0.0817^{+0.0131}_{-0.0167}$	505^{+325}_{-349}	0.9067	457
A2147	83074000	G2G3	19.4	0.0356	1.13	3.28	$5.45^{+0.51}_{-0.38}$	$0.21^{+0.03}_{-0.03}$	$0.0440^{+0.00536}_{-0.00686}$	119^{+46}_{-36}	1.0563	936
A2151	83030000	G2G3	18.2	0.0370	1.10	3.38	$3.04^{+0.43}_{-0.31}$	$0.39^{+0.10}_{-0.09}$	$0.0125^{+0.00431}_{-0.00790}$	173^{+53}_{-53}	0.9967	542
A2163	80024000	G2G3	16.0	0.2030	4.10	11.00	$13.28^{+0.75}_{-0.60}$	$0.18^{+0.03}_{-0.06}$	$0.0463^{+0.000485}_{-0.00152}$	0^{+169}_{0}	0.9218	838
A2199	80023000	G2G3	19.4	0.0299	0.96	0.87	$4.70^{+0.13}_{-0.15}$	$0.34^{+0.02}_{-0.02}$	$0.111^{+0.00654}_{-0.00419}$	130^{+23}_{-38}	1.0599	1077
A2204	82045000	G2G3	18.7	0.1523	3.87	5.61	$8.28^{+1.43}_{-1.02}$	$0.41^{+0.06}_{-0.05}$	$0.0400^{+0.00726}_{-0.00835}$	984^{+583}_{-653}	1.0396	657
	82045010	G2G3	17.7		3.67		$8.11^{+1.09}_{-0.79}$	$0.41^{+0.05}_{-0.05}$	$0.0442^{+0.00465}_{-0.00650}$	419^{+533}_{-419}	1.0443	699
	Combined						8.18 ± 1.08	0.41 ± 0.05	0.0425 ± 0.00669	665 ± 547		
A2218	80001000	G2G3	14.7	0.1710	3.32	3.34	$8.87^{+3.75}_{-1.74}$	$0.18^{+0.07}_{-0.07}$	$0.00947^{+0.00330}_{-0.00402}$	450^{+247}_{-329}	0.9975	585
A2219	82037000	G2G3	14.0	0.2281	3.88	1.75	$13.15^{+7.85}_{-3.37}$	$0.26^{+0.08}_{-0.07}$	$0.0172^{+0.00627}_{-0.0103}$	989^{+605}_{-850}	0.9247	680
A2255	84012000	G2G3	17.9	0.0808	2.20	2.60	$7.44^{+1.05}_{-0.68}$	$0.25^{+0.04}_{-0.04}$	$0.0257^{+0.00351}_{-0.00380}$	122^{+89}_{-101}	0.9644	912
	84012010	G2G3	16.9		2.08		$8.18^{+1.40}_{-0.91}$	$0.14^{+0.05}_{-0.04}$	$0.0241^{+0.00362}_{-0.00490}$	126^{+98}_{-94}	0.9742	820
	Combined						7.76 ± 1.01	0.20 ± 0.04	0.0250 ± 0.00396	124 ± 96		
A2256	10004030	G2G3	18.9	0.0581	1.73	4.30	$10.62^{+1.96}_{-1.20}$	$0.26^{+0.03}_{-0.03}$	$0.0485^{+0.00856}_{-0.0119}$	439^{+69}_{-67}	1.0256	1005
	80002000	G2G3	18.9		1.73		$8.03^{+0.57}_{-0.50}$	$0.27^{+0.02}_{-0.02}$	$0.0709^{+0.00495}_{-0.00548}$	200^{+66}_{-67}	1.0510	1090
	Combined						8.69 ± 1.06	0.27 ± 0.03	0.0633 ± 0.00772	318 ± 67		
A2261	84062000	G2G3	16.2	0.2240	4.44	3.28	$7.49^{+0.72}_{-0.41}$	$0.27^{+0.08}_{-0.08}$	$0.0189^{+0.000376}_{-0.00155}$	0^{+304}_{0}	1.1077	477
A2319	80041000	G2G3	19.4	0.0564	1.73	8.59	$13.27^{+2.06}_{-1.44}$	$0.27^{+0.04}_{-0.04}$	$0.120^{+0.0136}_{-0.0176}$	431^{+111}_{-106}	0.9574	1010
	80041010	G2G3	19.4		1.73		$14.11^{+3.62}_{-1.78}$	$0.27^{+0.04}_{-0.04}$	$0.113^{+0.0150}_{-0.0241}$	411^{+130}_{-112}	0.9441	976
	Combined						13.60 ± 2.22	0.27 ± 0.04	0.117 ± 0.0176	422 ± 115		
A2390	82032000	G2G3	13.3	0.1237	2.34	7.00	$15.32^{+84.68}_{-4.65}$	0.00 ± 0.07	$0.0163^{+0.00637}_{-0.0163}$	234^{+187}_{-234}	0.9685	299
	82032010	G2G3	14.2		2.50		$25.36^{+18.55}_{-14.01}$	$0.00^{+0.12}_{-0.00}$	$0.00577^{+0.0120}_{-0.00577}$	404^{+58}_{-270}	0.9836	241
	82032020	G2G3	11.8		2.07		$24.61^{+75.39}_{-13.41}$	$0.15^{+0.20}_{-0.15}$	$0.00715^{+0.0116}_{-0.00715}$	384^{+70}_{-279}	0.8473	164
	Combined						23.09 ± 35.12	0.02 ± 0.09	0.00928 ± 0.00987	348 ± 183		
A2440	81033000	G2G3	19.4	0.0904	2.63	5.16	$3.88^{+0.16}_{-0.14}$	$0.18^{+0.06}_{-0.06}$	$0.0191^{+0.000417}_{-0.000883}$	0 ± 53	1.0115	685
A2597	83062000	G2G3	16.5	0.0852	2.12	2.48	$3.91^{+0.27}_{-0.22}$	$0.31^{+0.04}_{-0.04}$	$0.0297^{+0.00303}_{-0.00347}$	259^{+176}_{-178}	1.1039	786
A2634	83002000	G2G3	19.4	0.0309	0.99	4.88	$3.27^{+0.17}_{-0.07}$	$0.28^{+0.05}_{-0.05}$	$0.0296^{+0.000585}_{-0.00256}$	0^{+23}_{0}	1.0121	769
A2657	84002000	G2G3	18.2	0.0414	1.22	6.00	$3.89^{+0.24}_{-0.15}$	$0.21^{+0.04}_{-0.04}$	$0.0369^{+0.00173}_{-0.00353}$	19^{+46}_{-19}	1.0637	870
A2670	82049000	G2G3	17.2	0.0759	2.00	2.69	$3.85^{+0.78}_{-0.25}$	$0.12^{+0.08}_{-0.08}$	$0.0170^{+0.00142}_{-0.00519}$	44^{+184}_{-44}	1.0187	524
A2811	84003000	G2G3	14.2	0.1090	2.25	1.54	$5.58^{+0.75}_{-0.41}$	$0.17^{+0.05}_{-0.05}$	$0.0169^{+0.00154}_{-0.00298}$	87^{+166}_{-87}	1.0739	733
A3112	81003000	G2G3	17.4	0.0746	2.00	4.00	$4.69^{+0.27}_{-0.26}$	$0.43^{+0.04}_{-0.03}$	$0.0414^{+0.00417}_{-0.00321}$	161^{+115}_{-161}	1.0023	870
A3158	84020000	G2G3	18.9	0.0575	1.72	1.20	$8.33^{+1.43}_{-0.95}$	$0.26^{+0.03}_{-0.04}$	$0.0302^{+0.00596}_{-0.00750}$	292^{+55}_{-59}	1.0262	921
A3221	83048000	G2G3	17.7	0.1044	2.71	2.66	$7.29^{+2.15}_{-1.15}$	$0.30^{+0.06}_{-0.06}$	$0.0165^{+0.00503}_{-0.00647}$	465^{+168}_{-214}	0.9831	629
A3266	83023000	G2G3	19.4	0.0545	1.68	3.00	$9.69^{+0.97}_{-0.92}$	$0.27^{+0.03}_{-0.03}$	$0.0699^{+0.00810}_{-0.00611}$	145^{+55}_{-86}	1.0256	1068
A3376	84056000	G2G3	18.9	0.0490	1.49	4.41	$4.38^{+0.36}_{-0.12}$	$0.22^{+0.05}_{-0.05}$	$0.0319^{+0.000538}_{-0.00394}$	0^{+63}_{0}	0.8903	621
A3391	72019000	G2G3	19.2	0.0540	1.65	4.50	$6.90^{+1.47}_{-0.86}$	$0.34^{+0.06}_{-0.06}$	$0.0261^{+0.00505}_{-0.00676}$	131^{+63}_{-66}	1.0424	669
A3526	80032000	G2G3	19.4	0.0107	0.36	7.96	$4.02^{+0.16}_{-0.14}$	$0.58^{+0.03}_{-0.03}$	$0.134^{+0.00884}_{-0.00998}$	56^{+8}_{-7}	1.1278	973
	83026000	G2G3	19.4		0.36		$4.06^{+0.08}_{-0.07}$	$0.53^{+0.01}_{-0.01}$	$0.139^{+0.00484}_{-0.00518}$	51^{+4}_{-4}	1.4433	1209
	Combined						4.04 ± 0.11	0.55 ± 0.02	0.137 ± 0.00721	53 ± 6		
A3558	82046000	G2G3	19.4	0.0476	1.48	4.00	$6.35^{+0.57}_{-0.46}$	$0.29^{+0.03}_{-0.03}$	$0.0771^{+0.00790}_{-0.00894}$	219^{+86}_{-87}	1.0764	847
	83058000	G2G3	19.4		1.48		$6.84^{+0.54}_{-0.45}$	$0.34^{+0.03}_{-0.03}$	$0.0591^{+0.00587}_{-0.00677}$	235^{+58}_{-58}	1.1824	944
	Combined						6.60 ± 0.50	0.32 ± 0.03	0.0668 ± 0.00737	229 ± 72		
A3562	84041000	G2G3	19.4	0.0478	1.49	4.20	$6.96^{+1.77}_{-0.95}$	$0.33^{+0.06}_{-0.06}$	$0.0253^{+0.00619}_{-0.00878}$	167^{+52}_{-57}	0.9570	661
A3571	82047000	G2G3	19.4	0.0390	1.23	4.04	$8.12^{+0.42}_{-0.39}$	$0.38^{+0.02}_{-0.02}$	$0.137^{+0.00692}_{-0.00749}$	130^{+44}_{-44}	1.0454	1125
A3627	84005000	G2G3	19.4	0.0164	0.54	20.20	$9.31^{+1.00}_{-0.67}$	$0.26^{+0.02}_{-0.02}$	$0.0819^{+0.0109}_{-0.0131}$	76^{+6}_{-7}	1.1666	1148

Table A2. Broad-Band Cooling Flow Spectral Fit Results – contd.

Object	Seq. Num.	Inst.	$A_{\rm out}$ (′)	z	$R_{\rm out}$ (Mpc)	$N_{\rm H}/10^{20}$ (cm^{-2})	$T_{\rm X}$ (keV)	Z (⊙)	Norm. ($\frac{10^{-14}}{4\pi D_{\rm L}^2}\int n_e n_{\rm H}dV$)	$\dot{M}$ (M$_\odot$ yr^{-1})	χ^2_ν	$N_{\rm PI}$
A3667	83054000	G2G3	19.4	0.0585	1.79	4.00	$8.11^{+0.82}_{-0.73}$	$0.25^{+0.03}_{-0.03}$	$0.0810^{+0.00867}_{-0.00880}$	196^{+106}_{-122}	0.9038	903
A3921	83048010	G2G3	18.2	0.0784	2.18	2.94	$9.96^{+7.83}_{-2.74}$	$0.19^{+0.08}_{-0.07}$	$0.0101^{+0.00771}_{-0.0101}$	319^{+55}_{-115}	0.9824	548
A4059	82030000	G2G3	19.4	0.0478	1.49	1.10	$4.05^{+0.23}_{-0.19}$	$0.49^{+0.04}_{-0.04}$	$0.0416^{+0.00282}_{-0.00360}$	51^{+65}_{-51}	0.9783	866
2A0336	82029000	G2G3	19.4	0.0350	1.12	17.20	$3.15^{+0.10}_{-0.08}$	$0.38^{+0.03}_{-0.03}$	$0.118^{+0.00597}_{-0.00674}$	75^{+89}_{-75}	1.0015	885
	82040000	G2	17.9		1.03		$3.08^{+0.09}_{-0.03}$	$0.37^{+0.03}_{-0.03}$	$0.118^{+0.000864}_{-0.00569}$	0^{+80}_{0}	1.0333	500
	Combined						3.11 ± 0.08	0.38 ± 0.03	0.118 ± 0.00482	24 ± 61		
AWM4	83072000	G2G3	17.2	0.0424	1.18	4.93	$2.41^{+0.20}_{-0.08}$	$0.29^{+0.09}_{-0.08}$	$0.0171^{+0.000915}_{-0.00273}$	11^{+65}_{-11}	1.1190	667
AWM7	80036000	G2G3	19.4	0.0176	0.58	9.19	$3.96^{+0.16}_{-0.14}$	$0.47^{+0.03}_{-0.03}$	$0.148^{+0.00818}_{-0.00903}$	29^{+23}_{-23}	1.0062	883
CL0016	80025000	G2G3	9.6	0.5500	4.25	3.21	$7.54^{+0.96}_{-0.64}$	$0.12^{+0.12}_{-0.12}$	$0.00599^{+0.000209}_{-0.000742}$	0^{+725}_{0}	1.0662	236
	84016000	G2G3	9.1		4.03		$8.83^{+1.81}_{-0.80}$	$0.35^{+0.12}_{-0.12}$	$0.00544^{+0.000177}_{-0.00120}$	0^{+1005}_{0}	0.8566	381
	Combined						8.03 ± 1.05	0.24 ± 0.12	0.00576 ± 0.000583	0 ± 432		
Cygnus-A	70003000	G2G3	19.4	0.0575	1.76	36.10	$37.03^{+2.89}_{-4.52}$	$0.94^{+0.04}_{-0.06}$	$0.00231^{+0.00917}_{-0.00231}$	564^{+14}_{-14}	1.1908	1111
	70003010	G2G3	19.4		1.76		$40.42^{+1.48}_{-1.74}$	$0.97^{+0.03}_{-0.06}$	$(8.88^{+907.}_{-8.88}) \times 10^{-05}$	531^{+11}_{-11}	1.4525	1177
	Combined						39.40 ± 2.66	0.96 ± 0.05	0.00108 ± 0.00516	545 ± 13		
Klemola44	83004000	G2G3	18.4	0.0283	0.86	1.56	$3.33^{+0.13}_{-0.11}$	$0.32^{+0.03}_{-0.03}$	$0.0576^{+0.00369}_{-0.00418}$	55^{+30}_{-29}	1.0187	936
MKW3s	80011000	G2G3	18.7	0.0434	1.31	2.89	$3.71^{+0.16}_{-0.19}$	$0.34^{+0.04}_{-0.04}$	$0.0432^{+0.00493}_{-0.00316}$	138^{+46}_{-80}	0.9554	776
MKW4s	83008000	G2G3	16.2	0.0288	0.77	1.66	$2.09^{+0.43}_{-0.24}$	$0.12^{+0.13}_{-0.06}$	$0.00780^{+0.00257}_{-0.00332}$	25^{+28}_{-25}	1.0008	508
MKW9	83009000	G2G3	12.5	0.0397	0.81	4.11	$1.88^{+0.40}_{-0.12}$	$0.24^{+0.15}_{-0.13}$	$0.00623^{+0.00120}_{-0.00155}$	14^{+63}_{-14}	1.0193	407
Ophiuchus	80027000	G2G3	19.4	0.0280	0.90	19.70	$12.74^{+0.30}_{-0.28}$	$0.35^{+0.02}_{-0.03}$	$0.516^{+0.00259}_{-0.00325}$	0^{+7}_{0}	1.0874	1166
PKS0745-19	81016000	G2G3	17.4	0.1028	2.63	35.00	$8.08^{+0.54}_{-0.46}$	$0.32^{+0.02}_{-0.02}$	$0.0808^{+0.00549}_{-0.00624}$	552^{+242}_{-238}	1.0102	1080
SC1327	83059000	G2G3	19.4	0.0476	1.48	4.00	$3.92^{+0.44}_{-0.32}$	$0.13^{+0.05}_{-0.05}$	$0.0322^{+0.00517}_{-0.00617}$	90^{+88}_{-90}	1.0395	724
Tri.Aus.	83060000	G2G3	19.4	0.0510	1.58	12.70	$11.61^{+1.72}_{-0.99}$	$0.26^{+0.04}_{-0.175}$	$0.154^{+0.0132}_{-0.0175}$	161^{+125}_{-113}	0.9848	1004
	83060010	G2G3	19.4		1.58		$16.59^{+9.63}_{-3.19}$	$0.32^{+0.07}_{-0.06}$	$0.100^{+0.0235}_{-0.0441}$	397^{+118}_{-122}	0.9539	756
	Combined						12.48 ± 3.88	0.28 ± 0.05	0.137 ± 0.0246	278 ± 119		
Virgo	60033000	G2G3	19.4	0.0036	0.12	2.50	$2.48^{+0.03}_{-0.03}$	$0.40^{+0.02}_{-0.02}$	$0.484^{+0.0129}_{-0.0133}$	5^{+1}_{-1}	1.3169	997
Zw3146	80014000	G2G3	9.1	0.2906	2.95	3.01	$7.63^{+2.63}_{-1.30}$	$0.38^{+0.08}_{-0.07}$	$0.0110^{+0.00421}_{-0.00525}$	2061^{+936}_{-1295}	1.0253	523

APPENDIX B: TEMPERATURE AND ABUNDANCE

PROFILE RESULTS

In the following figures we plot the averaged radial temperature and metallicity profiles (created using the procedure detailed in Section 3.0.1) for the 106 clusters in our sample. The y-axis data have 1-σ error bars, and the x-axis error-bars represent the extrema of the radii for each annular bin. Note, the bottom of each panel shows the radius in arcmin while the top shows the radius is Mpc assuming $H_0 = 50$ $\mathrm{km\,s^{-1}\ Mpc^{-1}}$, $q_0 = 0.5$.

The solid (heavier) diamond symbols with with diamond error bars are our averaged *SID* results. The triangle symbol with a dot-dashed line for the limits which cover the whole radial range of the data are the broad-beam fits to cooling flow model.

Results from Markevitch et al. (1998) (and the papers referenced therein which use the same method) [A85, A119, A399, A401, A478, A665, A754, A780, A1650, A1651, A1795, A2029, A2065, A2142, A2163, A2256, A2319, A2657, A3112, A3266, A3376, A3391, A3395, A3571, A3667, A4059, AWM7, Cygnus-A, MKW3s, A3558, Triangulum Australis] are shown by cross symbols with conventional error-bar limits as a dotted line. Additional data from *ROSAT* [A478, A1795, A3526] and Beppo-SAX [A426, A2319, Virgo] are shown by square symbols with a dashed line. (References for the *ROSAT* and Beppo-SAX data are given at the end of Section 3.)